# Atropisomerization of 8-Membered Dibenzolactam: Experimental NMR and Theoretical DFT Study

Alexei V. Buevich*

Merck Research Laboratories, Discovery and Preclinical Sciences, Process and Analytical Chemistry, NMR Structure Elucidation, Kenilworth, New Jersey 07033, United States

S *Supporting Information*

ABSTRACT: Detailed experimental and theoretical quantum mechanical analysis of the atropisomerization mechanism of a complex, bridged biaryl molecule with imbedded biphenyl, amine, and lactam moieties, 7,8-diallyl-5-benzyl-7,8-dihydrodibenzo[e,g][1,4]diazocin-6(5H)-one (**1**), was undertaken. Experimental Gibbs free activation energy, activation enthalpy, and activation entropy were established by temperature-dependent kinetic NMR experiments. Theoretical analysis utilized density functional theory (DFT) calculations at the B3LYP/6-31G(d) level of theory. Twelve energy minima and 17 transition states associated with five different atropisomer interconversion pathways were found by the combination of DFT calculated two-dimensional potential energy surfaces (2D PES) and the quadratic synchronous transit-guided (QST2) method. Among the five possible atropisomerization pathways, the lowest Gibbs free activation energy 25.8 kcal/mol was in close agreement with the experimentally determined value of 26.8 kcal/mol. Theoretical activation entropies and enthalpies were also consistent with experimental data. Geometrical and vibrational analysis of transition states and metastable intermediates suggested the mechanism of atropisomer interconversion of **1** as a rotation of the eclipsed endocyclic coordinate in a clockwise or counterclockwise direction along the ring. Puckering ability at least in one of the segments of the ring appears to be one of the most critical factors defining the height of atropisomerization barrier.

NMR: $\Delta G_{298}^{\ddagger} = 26.8$ kcal/mol

DFT: $\Delta G_{298}^{\ddagger} = 25.8$ kcal/mol
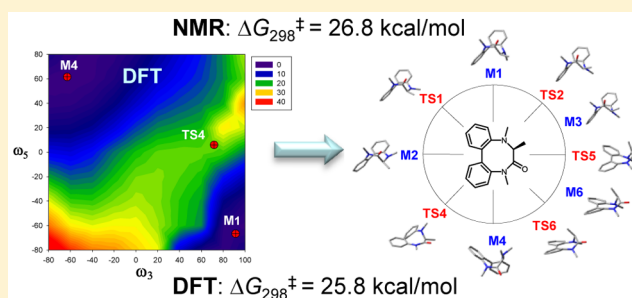
INTRODUCTION

Biaryl moieties remain one of the most captivating structural motifs. Thus, biaryls can be frequently found in pharmacologically active natural products (e.g., vancomycin,[1a] steganone,[1b] michellamine[1c]) and synthetic drugs (e.g., losartan,[2a,b] valsartan,[2b] irbesartan,[2b] candesartan[2b]). In medicinal chemistry biaryls are classified as one of the so-called privileged structures, i.e., a single molecular framework able to provide high-affinity ligands for more than one type of receptors.[3] Axial chirality of biaryl systems have been widely employed in synthetic organic chemistry where they are frequently used as chiral auxiliaries and catalysts to transfer a chirality.[4] Biaryl structures have also been utilized in molecular electronics devices as a single molecule junction with robust structure−conductance relationship.[5]

When biaryls have bulky substituents in ortho positions they are prone to atropisomerism, a stereoisomerism property defined by the high (>25 kcal/mol) barrier of rotation about the sp^2−sp^2 carbon−carbon bond.[6] At such high kinetic barriers, conformational exchange becomes extremely slow (hours to days), which facilitates the separation at ambient temperatures of individual conformers (atropisomers) with potentially different biological, pharmacological, and catalytic properties. In this context, we believe that the detailed structural and mechanistic analysis of the atropisomerization

process provides invaluable insights that can improve drug development,[7] organic catalysis,[4] molecular electronics development,[5] and other fields where atropisomers playing an important and prevalent role.

Experimental and theoretical studies of atropisomerization of open-chain (linear) biaryl scaffolds are well documented.[4,8,9] It is only the tri- and tetra-ortho-substituted open-chain biaryls that exhibit atropoisomerism since it is only in these systems that ortho substituents would experience a significant steric repulsion in the transition state. The twist angle between the two aromatic rings is mainly a result of the two competing effects: repulsion of ortho substituents and π-system conjugation. While in biphenyl the twist angle is close to 45°, in other biaryls it varies dramatically and is a function of the number, position, and type of substituents. The transition state of atropisomer interconversion is close to a planar form, but with severely distorted chemical bonds of both ortho substituents and aromatic rings. Overall, the mechanism of atropisomerization of open-chain biaryls can be described by a single transition state, and it can be theoretically modeled by a single torsion angle coordinate (twist angle). In cyclic (bridged) biaryls the atropisomerism

can be attained with only two ortho substituents provided that the needed extra rigidity arises from geometrical restrictions of the ring. Interestingly, despite considerable experimental data on cyclic biaryl atropisomers,[4,10] there is nevertheless only very limited research published on a mechanism of their interconversion.[4b,11] This discrepancy can be explained by the apparent difference between open-chain and cyclic systems. While atropisomer interconversion of linear biaryls can be described by a single torsion angle coordinate, in cyclic structures it becomes a function of multiple endocyclic torsion angles. Furthermore, in cyclic biaryls, it is not known whether one or multiple transitions states are en route from one atropisomer to the other, whether the highest barrier can be attributed to the interaction of the two aryl groups and what the sequence of transitions that governs and mediates the overall process of atropisomerization.

The goal of the current study was to examine, perhaps for the first time, the mechanism of atropisomerization of a complex, bridged biaryl molecule with imbedded biphenyl, amine, and lactam moieties. Recently, we have reported the synthesis and initial structural analysis of such a structure, 8-membered dibenzolactam 7,8-diallyl-5-benzyl-7,8-dihydrodibenzo[e,g][1,4]diazocin-6(5H)-one (1).[12] Experimental NOE data and molecular modeling by force field calculations showed that 1 has two stable boat-like conformations that were classified as atropisomers based on very slow interconversion rates, even at 65 °C.[12a] Our initial attempts to estimate the energy of the transition states based on the driving coordinate method and force field calculations failed for the reasons that will be described below. In this study, we have attempted a more rigorous experimental and theoretical investigation of the mechanism of atropisomerization of 1. Experimental atropisomerization barriers of 1 were measured by a variable-temperature kinetic NMR experiment. Experimental Gibbs free activation energies, activation enthalpies, and entropies were then compared with values theoretically predicted by quantum mechanical density functional theory (DFT) calculations. The choice of DFT level of theory was needed due to the complexity of the studied system and was based on the notion that DFT calculations give reliable estimates of molecular geometries and energy barriers comparable in accuracy with those by *ab initio* post-Hartree–Fock methods.[13] The exhaustive search of transition states of 1 was also done at the DFT level. Multiple 2D potential energy surfaces (PES) of 1 were reconstructed by DFT calculations, which helped to locate more accurately numerous stationary points (energy minima and transition states) related to atropisomer interconversion. We believe that this study provides useful insights to a general mechanism of cyclic biaryls atropisomerization as well as the basis for better understanding of other molecules that share cores similar to that of 1, such as structural similarity naturally occurring steganone[1b] and synthetic potent γ-secretase inhibitor LY-411575, a prospective drug candidate for Alzheimer's disease.[10]

RESULTS AND DISCUSSION

Atropisomer Nomenclature. In the current study, two atropisomers of 1 are designated as (P,S) and (M,S) diastereomers in accordance with the axial chirality of the biphenyl substructure (P and M)[4b] and the S center chirality of the C3 carbon (Figure 1). Strictly speaking, 1 is a racemic mixture at the C3 carbon (S and R), and it therefore has two
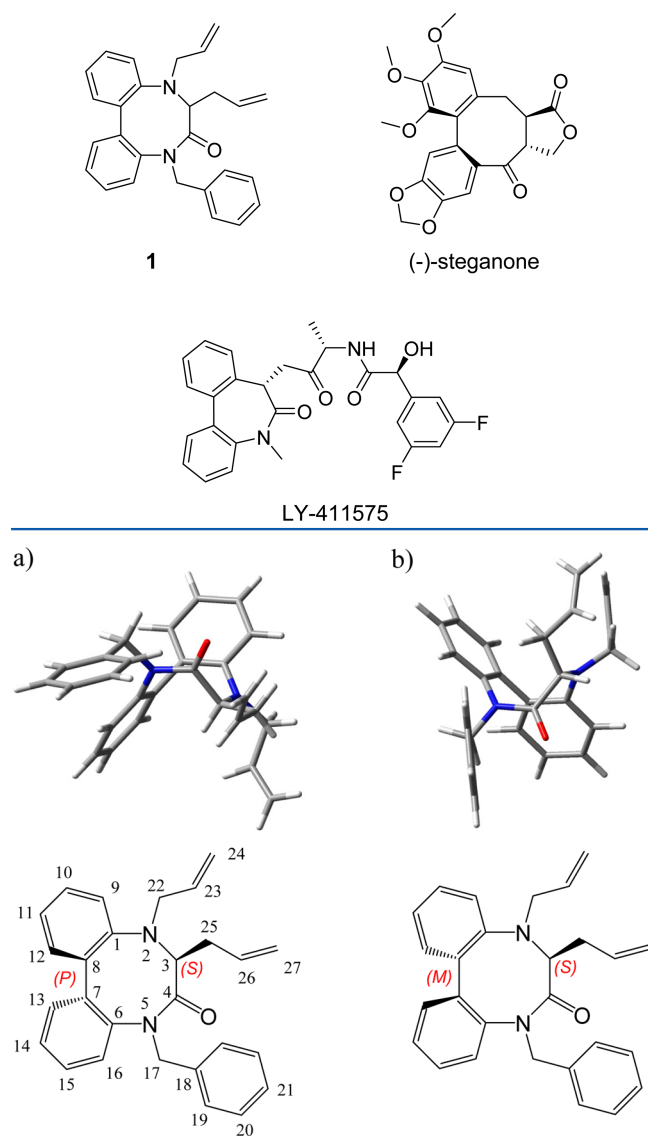

Figure 1. (a) (P,S) and (b) (M,S) atropisomers of 1. Minimum energy conformations of (P,S) and (M,S) by force field calculations[12a] are shown on the top.

pairs of diastereomers (i.e., (P,S),(M,S) and (M,R),(P,R)). However, considering that 1 was studied in an achiral solvent (toluene-d_8), the mechanisms of interconversion for each of these pairs are identical and, therefore, without any loss of generality for our study can be limited to one pair of atropisomers, for example, (P,S) and (M,S).

EXPERIMENTAL KINETICS

Atropisomer interconversion at three temperatures (34.2, 47.8, and 61.4 °C) was investigated by ^{1}H NMR spectroscopy. Specifically, the integral intensity of the H9 protons resonances of two atropisomers at 6.3–6.5 ppm were used to monitor the kinetics of atropisomer interconversion (Figure 2). Analysis of those data were done in approximation of the first-order exchange mechanism (M,S)↔(P,S) (see the Experimental Section), resulting in the set of rate constants shown in Table 1. Kinetic rates were subsequently analyzed by using the Eyring equation[14] to give the free-energy parameters of atropisomer interconversion as summarized in Table 2.

Table 1. Exchange Rate Constants and Gibbs Free Activation Energies of (P,S) and (M,S) Atropisomers of 1 in Toluene-d_8

T (°C)	n^a	RMSD^b	$k_{MP} \times 10^5$ (s^{-1})	$k_{PM} \times 10^5$ (s^{-1})	$\Delta G_{MP}^{\ddagger}$ (kcal/mol)	$\Delta G_{PM}^{\ddagger}$ (kcal/mol)
34.2	65	0.000597	0.3521 ± 0.0004	0.0499 ± 0.0008	25.68 ± 0.01	26.87 ± 0.02
47.8	51	0.001024	1.843 ± 0.003	0.338 ± 0.003	25.79 ± 0.01	26.87 ± 0.01
61.4	66	0.002558	8.084 ± 0.016	1.426 ± 0.006	25.92 ± 0.01	27.07 ± 0.01

^{a}Number of time points. ^{b}Root-mean-square deviation: RMSD = $(\Sigma(y^{teor} - y^{exp})^2/(2n - 4))^{1/2}$, where y^{teor} and y^{exp} are theoretical and experimental normalized intensities of proton resonances, respectively (Figure 2).
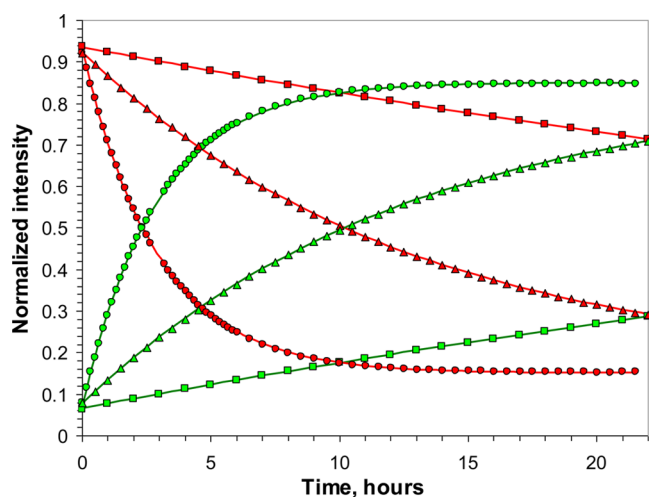

Figure 2. Exchange kinetics of the (M,S) (red) to (P,S) (green) atropisomers of **1** at 34.2 (squares), 47.8 (triangles), and 61.4 °C (circles) in toluene-d_8 measured by ^{1}H NMR. The curves are the best fit to the experimental data in approximation of the first-order kinetics.

Table 2. Experimental Gibbs Free Activation Energies, Activation Enthalpy, Activation Entropy, and Relative Gibbs Free Energies of 1 in Toluene-d_8

	$\Delta G_{298}^{\ddagger}$ (kcal/mol)	$\Delta H^{\ddagger}$ (kcal/mol)	$\Delta S^{\ddagger}$ (cal/K mol)	ΔG_{PM}^{0} (kcal/mol)
(M,S) to (P,S)	25.59 ± 0.02	22.9 ± 0.2	−9.0 ± 0.7	−1.18 ± 0.04
(P,S) to (M,S)	26.77 ± 0.02	24.5 ± 0.4	−7.6 ± 1.1	

As seen from Table 2, the measured free activation energies of (P,S) to (M,S) exchange of 25.6−26.8 kcal/mol are quite consistent with generally observed barriers for atropisomers exchange.[6] Relative Gibbs free energy of the (P,S) form is 1.18 kcal/mol lower than that of the (M,S).

Energy Minima of 1. The ensemble of the lowest energy conformations of **1** was generated with the help of in-house tools based on molecular mechanical conformation generator programs and geometry optimization by DFT.[15] Three programs, ET,[16] JG,[17] and OMEGA,[18] were used to generate up to 4500 conformations, which were subsequently ranked in conformational clusters. In total, 150 representative conformations have been reoptimized at the DFT level (B3LYP/6-31G(d)), and Gibbs free energies were calculated. After redundant forms were removed, a final set of 105 conformations of **1** was composed of 72 (P,S) and 33 (M,S) atropisomers (Figure 3).

Boltzmann distribution of the 105 conformations of **1** showed a 98.85:1.15 ratio of (P,S) to (M,S) which corresponded to an average 2.6 kcal/mol energy preference of (P,S) over (M,S) forms. The latter value was consistent overall with that determined experimentally ($\Delta G_{PM}^{0} = -1.18$ kcal/mol). A more accurate estimation of the relative free Gibbs energies of (P,S) and (M,S) atropisomers was found when free energies of 105 conformations were calculated with the dispersion-corrected B3LYP-D2 functional and 6-31G-(d,p) basis set ($\Delta G_{PM}^{0} = -1.28$ kcal/mol) (see the Supporting Information).

Choosing a Molecular Model and the Space of Conformational Variables for Transition-State Analysis. Identifying transition states is an immensely more difficult task than finding energy minima.[19] To discover a transition state, one would need to know a minimum energy path (MEP) between the two energy minima. The highest point on this path, also known as the saddle point, is the transition state (TS).[19] Requirements for the initial "guess" for TS optimization are much tighter than those of the energy minima; hence, a detailed knowledge of the path around the TS is highly desirable. A number of methods has been developed to search and optimize the TS, including linear and quadratic synchronous transit (LST, QST), coordinate driving, walking up valleys, reaction pathway approach, etc.[19] Among these approaches, it appears that the driving coordinate
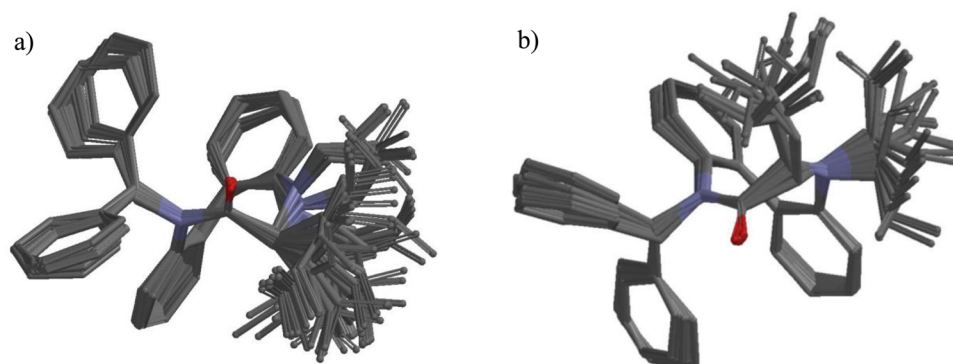

Figure 3. Ensembles of 72 (P,S) (a) and 33 (M,S) (b) conformations of **1**.
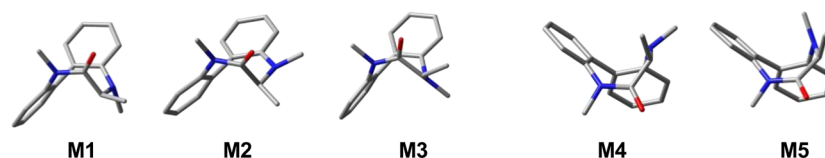
Figure 4. (*P,S*) (M1, M2, and M3) and (*M,S*) (M4, M5) conformations of **2**. The lowest energy conformations in two stereochemical families are M1 and M4 (see more detailed characterization of M1−M5 forms in the "energy minima" section).

method is the most suited for searching TS's in the conformational analysis.[20] However, this approach can have serious pitfalls even in a relatively simple case such as the inversion of the cyclohexane ring.[21] To overcome such pitfalls, the analysis of potential energy surfaces (PES) is required. On the other hand, the major problem of the PES analysis is its high dimensionality, which inevitably leads to substantial computational costs. To minimize these costs, a rational selection of key (dominant) coordinates for PES scanning is essential.

Since the main focus of the current study was the atropisomerism of the 8-membered ring inversion of **1**, we have considered a simpler molecular model, which would retain essential elements of the 8-membered dibenzolactam ring and simultaneously simplify the search of the transition states related only to the 8-membered ring. Assuming that the rotamer exchange of the 8-membered ring side chains at N2, C3, and N5 (one benzyl and two allyl groups) is independent from the ring interconversion, and noticing that these substituent groups do not bear charges, which would create nonbonded electrostatic interactions potentially affecting ring interconversion, it was reasonable to suggest that the analysis of the ring interconversion of **1** could be modeled on the reduced structure **2**, in which the benzyl and two allyl groups of **1** were approximated by methyls:
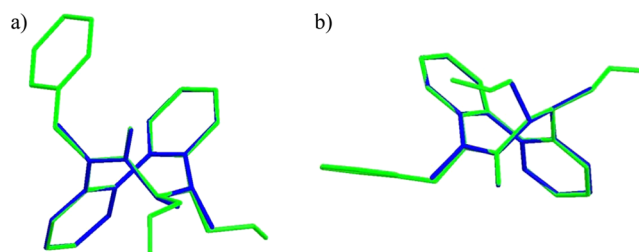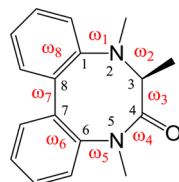

2

Analogous to **1**, the initial search of energy minima of **2** was done via a combination of molecular mechanical conformational generators and DFT optimization steps as described above. This analysis afforded only three (*P,S*) and two (*M,S*) conformations (Figure 4), among which the M1 and M4 forms had the lowest energies (see more detailed characterization of M1−M5 forms in the "energy minima" section). In the present work, all energy minimum conformations are labeled as M forms and transition states as TS forms.

Spatial overlay of the lowest energy conformations of **1** and **2** revealed a nearly perfect match of their 8-membered rings (Figure 5). This observation strongly supported the premise that the orientation of the side chains in **1** has a minimal effect on ring geometry and also strengthened the hypothesis that the effect of side chains on the ring's transition states was minimal and could be disregarded.

Thus, switching to the model structure **2** enabled us to reduce the number of rotatable bonds, which led to a distinct

Figure 5. Superposition of the most stable conformations of **1** (green) and **2** (blue) of (a) (*P,S*) and (b) (*M,S*) atropisomers.

simplification of the conformational space from 105 to five members only.

The search for transition states is usually done in the internal coordinate space, represented by bond lengths, bond angles, and torsion angles.[19b] The 38 atom molecule of **2** possesses 108 degrees of freedom (3 × 38 − 6) in internal coordinate space. As the conformational exchange of a ring system is mainly limited to a torsion angle perturbation, with a much lesser effect on bond lengths and angles, it was rational to restrict the space of tested variables to eight endocyclic torsion coordinates (ω_i, i = 1, 2, ... 8).

The endocyclic torsion angles in **2** have been further ranked as dominant or nondominant. That classification was made on the basis of the extent of perturbation that each of the torsional angles was subjected to upon atropisomer interconversion. As seen from Figure 6, in which differences
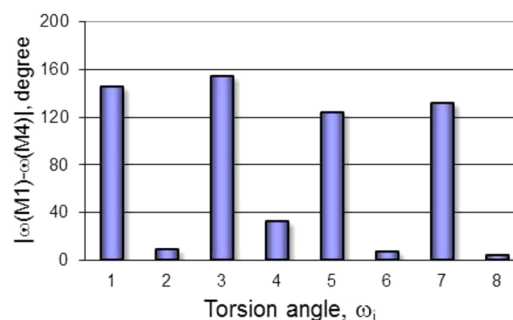

Figure 6. Difference of ring torsion angles (absolute values) between lowest energy (*P,S*) and (*M,S*) atropisomers of **2**. Torsion angles with largest amplitudes were classified as dominant (ω_1, ω_3, ω_5, and ω_7), whereas small amplitude angles were classified as nondominant (ω_2, ω_4, ω_6, and ω_8).

of the ring torsion angles between lowest energy (*P,S*) (M1) and (*M,S*) (M4) atropisomers are shown, the four angles, ω_1, ω_3, ω_5, and ω_7, proceed through substantial perturbations in the range of 120−160°. These four angles were classified as dominant and later have been chosen as key variables for potential energy surface scans.

The remaining four nondominant endocyclic torsional angles had much smaller perturbations upon the ring
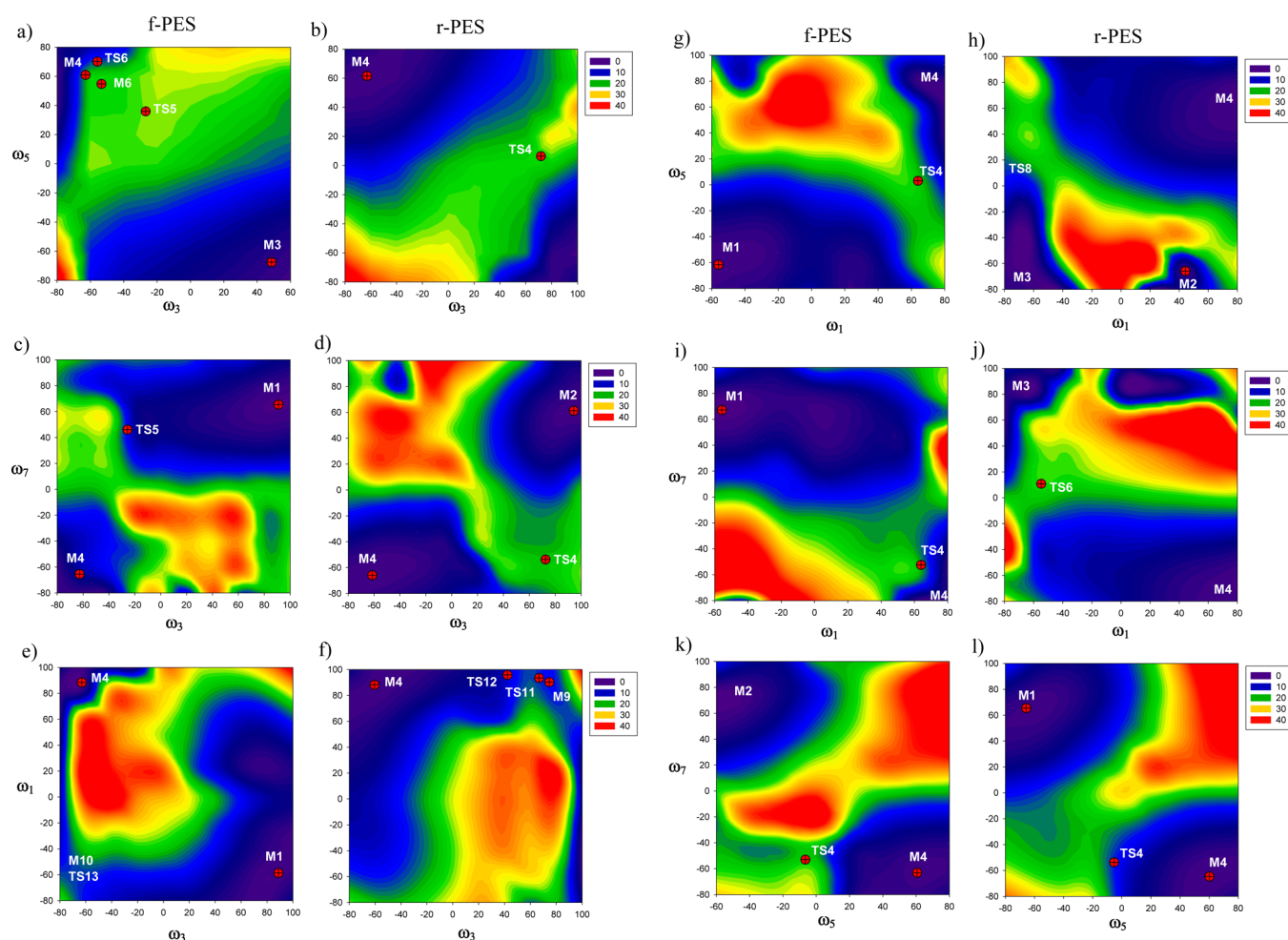
Figure 7. 2D PES of the M1 to M4 interconversion in the (ω_3, ω_5), (ω_3, ω_7), (ω_3, ω_1), (ω_1, ω_5), (ω_1, ω_7), and (ω_5, ω_7) coordinate space. For each pair of coordinates two 2D PESs, one driven from the M1 to (M,S) (f-PES) and another from the M4 to (P,S) (r-PES), were calculated at the DFT level of theory (B3LYP/6-31G(d)) on a 20° grid. Red markers show the coordinates of stationary states on each PES found by unconstrained optimizations.

interconversion, consistent with geometric constraints imposed upon them by two phenyl rings (ω_6 and ω_8) and by the C4−N5 amide bond (ω_4). The only torsional angle that was not constrained by any embedded group, but has the same sign and nearly the same value in both lowest energy atropisomers, was ω_2. At this point, that angle was placed into the nondominant category, although a subsequent analysis showed its rather unique and critical role, as discussed below.

Thus, the mechanism of atropisomer interconversion of **1** was explored in the space of the four dominant endocyclic torsion angle coordinates of the model molecule, **2**. En route from one atropisomer to the other, each of these coordinates has to pass a zero value (i.e., the eclipsed angle). In linear molecules, conformations with eclipsed angles are usually associated with the structure of the transition state. If this assumption holds for cyclic systems, then one would expect up to four transition states in the case of **2**. However, in cyclic structures, internal torsion angle coordinates are strongly correlated with each other, making it more problematic to predict the total number of transition states. If there were several transition states, then it is also unknown how these transitions states are passed: simultaneously, sequentially, or randomly. The most complete and exhaustive answers to

these questions can be found from the analysis of potential energy surfaces.

Potential Energy Surfaces (PES). Initial attempts to identify transition state (states) of **2** by driving one of the four dominant torsion angles between the values of the two lowest energy atropisomeric forms (M1 and M4) were unsuccessful. The one-dimensional driver approach did not allow the passage over the transition state. Instead, it led to high energy conformations with greatly distorted geometries. Therefore, in the current study, we employed a two-dimensional driver approach wherein a pair of dominant torsion angles was simultaneously driven. In the two-dimensional driver approach, passing through transition states was achieved for any given combinations of the four dominant angles. On the basis of that approach, exploratory potential energy surfaces in a two-dimensional space of endocyclic torsional coordinates were constructed.

There are six possible pairs of four dominant angles of **2** (i.e., (ω_1, ω_3), (ω_1, ω_5), (ω_1, ω_7), (ω_3, ω_5), (ω_3, ω_7), and (ω_5, ω_7)). Since the shape of the PES depends on the direction in which it is scanned,[22] 12 PES's where calculated including six forward driven PES (f-PES) from M1 to M4 and six reverse driven PES (r-PES) from M4 to M1 structures. 2D contour plots of 12 PES's marked with the positions of

Table 3. Torsion Angles and Gibbs Free Energies of Stationary Points of 2

form	ω_1	ω_2	ω_3	ω_4	ω_5	ω_6	ω_7	ω_8	G_{298}^0 (hartree)	ΔG_{298}^0 (kcal/mol)
M1	−57.7	−19.4	92.1	−14.6	−63.1	−0.2	66.1	4.0	−843.10839	0.00
M2	−13.3	−69.2	94.9	13.6	−63.8	−11.5	62.0	0.9	−843.10487	2.21
M3	−95.4	38.8	52.0	−13.5	−67.1	12.5	59.3	−0.7	−843.10608	1.45
M4	87.8	−28.4	−61.7	17.7	60.7	−6.7	−65.0	−0.4	−843.10718	0.76
M5	96.6	−50.3	−23.1	−14.1	78.3	−12.5	−56.7	−1.9	−843.10020	5.14
M6	−64.1	123.9	−54.1	−29.2	54.4	−26.3	30.0	−15.4	−843.06839	25.10
M7	−84.4	61.8	59.4	−114.8	38.1	−13.8	47.0	−11.5	−843.07833	18.86
M8	−74.7	59.7	44.4	−128.9	59.7	13.3	−19.8	20.2	−843.06341	28.23
M9	89.1	−85.7	77.1	−111.6	83.3	8.2	−54.9	−5.9	−843.08385	15.40
M10	−88.2	80.2	−70.9	110.1	−84.8	−7.7	55.5	5.9	−843.07731	19.50
M11	−93.6	89.1	−68.7	106.1	−88.5	−3.8	55.9	1.7	−843.07411	21.51
M12	86.6	−67.2	−51.3	112.3	−40.7	15.3	−47.1	10.8	−843.06894	24.76
TS1	−43.7	−32.4	102	−15.6	−53.9	−6.8	72.3	−0.6	−843.10275	3.54
TS2	−81.1	15.8	72.8	−19.1	−63.7	7.8	64.6	0.0	−843.10482	2.24
TS3	97.6	−39.5	−42.5	−0.3	76.3	−13.3	−56.5	−2.7	−843.09997	5.28
TS4	63.8	−130.9	72.6	−16.9	4.3	12.1	−53.4	26.3	−843.06723	25.83
TS5	−72.8	113.8	−26.6	−41.4	34.7	−16.9	45.4	−21.5	−843.06490	27.29
TS6	−52.8	117.4	−56.7	−38.2	71.4	−22.2	11.2	−11.9	−843.06667	26.18
TS7	63.8	−118.0	67.6	−14.4	−0.6	21.4	−55.7	22.3	−843.06258	28.75
TS8	−87.8	56.8	64.0	−94.9	10.9	−2.2	53.7	−13.2	−843.07598	20.34
TS9	−80.0	60.8	47.3	−128.6	56.7	9.3	−10.1	17.6	−843.06124	29.59
TS10	33.2	−7.7	48.0	−124.3	70.4	27.2	−48.8	−19.4	−843.04849	37.59
TS11	92.3	−85.6	73.5	−116.9	88.6	10.2	−55.2	−8.5	−843.07898	18.46
TS12	98.6	−81.2	41.6	−78.2	97.4	−6.7	−52.5	−4.1	−843.07510	20.89
TS13	−88.1	81.2	−71.7	115.9	−87.3	−10.1	55.6	6.4	−843.07543	20.69
TS14	−93.5	90.6	−68.9	106.6	−88.3	−3.3	54.7	0.3	−843.07327	22.04
TS15	20.2	−32.7	−37.3	123.8	−67.1	−25.3	48.8	−8.1	−843.04288	41.11
TS16	89.2	−64.0	−57.1	103.3	−24.1	8.2	−51.1	11.8	−843.06633	26.39
TS17	81.1	−69.5	−35.9	124.1	−60.6	−6.4	6.6	−14.5	−843.05270	34.94

optimized stationary points are shown in Figure 7. It is noteworthy that for each pair of direct and reverse PES's, if one rotates one of the surfaces around the C_2 (z) axis then the two would be nearly superimposable. The apparent symmetry of the two PES's might suggest that they describe the same pathway and their calculations would therefore be redundant. However, most pairs of forward and reverse driven PES's established different pathways (see labels of transition states in Figure 7).

Overall, 2D PES's have smooth shapes with often a single, rather narrow ridge, consequently suggesting the existence of a single transition state between the two atropisomers. However, the subsequent analysis showed multiple transition states along a single path, and the exact coordinates of optimized TS states, designated with red markers in Figure 7, often deviated from those projected by a minimum energy paths suggested by the PES shape. That apparent discrepancy was caused by constrained conditions at which PES's were calculated and by the relatively low resolution of the PES grid (20°). Therefore, it is important to specifically note that the PES scans were primarily used to localize a saddle point on the ridge, which provided a starting geometry for unconstrained optimization in the space of all internal variables.

The analysis of transition states with the help of PES scans can be illustrated on the following example. The shape of the (ω_3, ω_5) r-PES plot (Figure 7b) suggested the approximate position of the saddle point at the $(60°, 0°)$ coordinates. Transition-state optimization of that geometry resulted in the $(72.6°, 4.3°)$ transition state (TS4). In accordance with the procedure described in the Experimental Section, each of the

transition states then served as a starting point in the following energy minimization to afford local energy minima that were separated by a given TS state. Thus, the TS4 was determined to be the transition state between the M2 and M4 structures, where the M2 was not a global minimum. The transition states between two minima with close geometries, such as the TS1 state between the M1 and M2, were determined with the help of the quadratic synchronous transit-guided method (QST2),[23] which is well suited for this type of situation.

Opposite to the reverse driven (ω_3, ω_5) r-PES, the forward driven (ω_3, ω_5) f-PES shape (Figure 7a) has a large high energy plateau in the upper left quadrant, which indicated the possibility of multiple transition states in that region. That supposition was confirmed when a trial transition state at $(−60°, −20°)$ converged to the geometrically distinct $(−26.6°, 34.7°)$ structure of TS5. Subsequently, TS5 was determined to be the transition state between the M3 and M6 conformations. Finally, the QST2 search established the TS6 $(−56.7°, 71.4°)$ and TS2 $(72.8°, −63.7°)$ transition states between the M6 and M4 and between the M1 and M3 forms, respectively (Figure 7a). As indicated in Figure 7, transition states TS4, TS5, and TS6 were also identified on seven other 2D PES scans: (ω_3, ω_7) f-PES, (ω_3, ω_7) r-PES, (ω_1, ω_5) f-PES, (ω_1, ω_7) f-PES, (ω_1, ω_7) r-PES, (ω_5, ω_7) f-PES, and (ω_5, ω_7) r-PES.

It is noteworthy that the analysis of (ω_3, ω_1) f-PES, (ω_3, ω_1) r-PES, and (ω_1, ω_5) f-PES (Figures 7e, f, h) led to a new type of energy minimum conformation with a *trans*-amide C4−N5 bond, which was completely missed by the
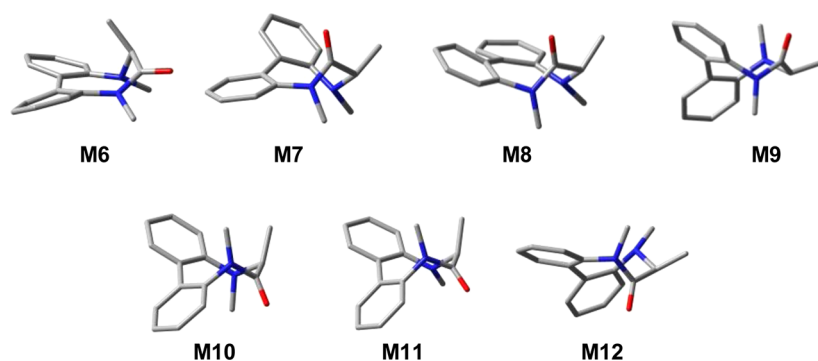
Figure 8. High energy conformations of **2**.

conformational search. The energy minimum form M10 and the transition state TS13 were identified on the forward-driven (ω_3, ω_1) f-PES, and the M9, TS11, and TS12 states were found with the help of the reverse-driven (ω_3, ω_1) r-PES scan. Discovery of these stationary points with the *trans*-amide bond was followed by a systematic QST2 analysis, which resulted in a number of additional energy minima and transition states. To probe the atropisomer interconversion through *trans*-amide conformations, four additional PES's were calculated. These results are further discussed in the next section. Geometrical and energetic parameters of all stationary points of **2** found through the analysis of PES scans and QST2 analysis are summarized in Table 3.

Energy Minima. Energy minimum states of **2** can be subdivided into four groups of structurally related conformers. The first group is composed of the boat M1 and twist-boat M2 and M3 conformations of the same (*P,S*) configuration (Figure 4). Naming of conformations of **2** was done on the basis of Hendrickson's notations for cyclooctane.[24]

The M1 conformations represents a global minimum of **2**, and the M2 and M3 structures are less stable than M1 by 2.23 and 1.44 kcal/mol (ΔG_{298}^0), respectively. The structural difference between the M1 and the M2, M3 forms is in the orientation of the N2 nitrogen lone electron pair, which is synclinal with the C4 carbonyl group in the M1 and anticlinal in the M2 and M3. Additionally, the M3 conformation differs from the M1 and M2 forms by the sign of the ω_2 torsion angle, which is positive in the M3 and negative in the M1 and M2 forms. The M2 and M3 forms are gauche conformers of the methyl groups at the N2 nitrogen and C3 carbon atoms with −41.3° and +56.4° torsion angles, respectively.

The M4 and M5 forms constitute the second group of twist-boat (*M,S*) conformations (Figure 4). Relative Gibbs free energies of these forms are 0.76 and 5.14 kcal/mol, respectively, and they represent the second most populated forms of **2**. Similar to the M1 and M2 conformations, the M4 and M5 forms have opposite orientations of the N2 nitrogen lone electron pair (Figure 4).

The third group combines the *trans*-amide bond conformations of both configurations: (*P,S*) (M7, M10, and M11) and (*M,S*) (M8, M9, and M12) (Figure 8). Most of the *trans*-amide conformations have a boat–chair form, except M8, which closely resembles the twist-boat–chair conformation.

The relative Gibbs free energies of the *trans*-amide forms are predicted to be in a range between 15.4 and 28.2 kcal/mol (Table 3), which is significantly higher than the energy range of the *cis*-amide conformations of the first two groups. In an

acyclic structure, cis and trans tertiary amides are expected to have very similar energies. However, in a medium-sized ring, such as **2**, the lowest energy conformation with a pure *trans*-amide bond ($\omega_4 = 180°$) cannot be attained due to the constraint of the ring system. Thus, in **2**, the amplitudes of the *trans*-amide ω_4 torsion angle are found in the 106.1–128.9° range (Table 3), which indicates a lesser degree of conjugation between the nitrogen lone electron pair and the carbonyl group. As a result of that, there will be extra strain energy as compared with a less strained, more conjugated, *cis*-amide conformations ($|\omega_4| \sim 13.5–17.7°$). Similar to the conformations of the first two groups, the *trans*-amide M10 and M11 forms are different in the orientation of the N2 nitrogen lone electron pair. It is interesting to note that, in contrast to the *cis*-amide conformations, the lowest energy *trans*-amide form has (*M,S*) configuration (M9). The distant second to that is the (*P,S*) M7 form, which lies 3.36 kcal/mol higher.

Another important feature of *trans*-amide conformations is the sign of the ω_4 angle, which is negative in M7, M8, and M9 and positive in M10, M11, and M12. Since within each of these subgroups there are forms that belong to different symmetries of the biphenyl fragment, one may also consider the (*P,S*)↔(*M,S*) atropisomer exchange where each of the states conserves the *trans*-amide bond sign. These possible pathways are discussed below.

The last group of energy-minimum conformations of **2** has only one member, the twist-boat–chair M6 form that has the (*P,S*) configuration and one of the highest energies among all energy minimum states (25.10 kcal/mol). Although the amide bond in this form is cis, on average, the shape of the M6 conformation is much flatter (except for the ω_2 angle) than that of any of the other energy minimum states (Table 3). The M6 form is a metastable intermediate between the TS5 and TS6 transition states. Being structurally similar to these two transition states, the M6 form has multiple torsional and bond angle distortions which ultimately contribute to its high energy.

In summary, one may conclude that only five conformations of the first two families are populated at room temperature. The probability of finding any other conformation at room temperature is infinitesimally small (3.7 × 10^{-10}%), and no effect on the observable energetic parameters is expected from these forms.

Atropisomer Interconversion via *cis*-Amide Transition States. The most relevant transition states related to the atropisomer interconversion of **2** are those between the most populated *cis*-amide conformations (M1–M5). Analysis of the

2D PES's combined with the QST2 searching algorithm identified three different pathways of atropisomer interconversion of **2** mediated by seven transition states (TS1−TS7) and one high-energy metastable intermediate M6 (Figure 9):
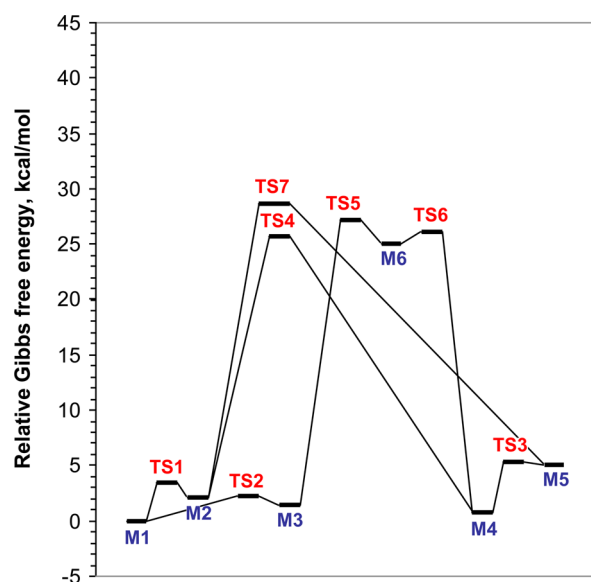

Figure 9. Energy profile for atropisomer (*P,S*) (M1, M2, M3, and M6 structures) interconversion with atropisomer (*M,S*) (M4, M5 structures) of **2**. Six energy minima and seven transition states (TS1−TS6) of **2** constitute three pathways with the TS4 state (25.83 kcal/mol) being the lowest barrier among all other barriers separating the (*P,S*) and (*M,S*) interconversion.

Path I: M1−TS1−M2−TS4−M4
Path II: M1−TS1−M2−TS7−M5−TS3−M4
Path III: M1−TS2−M3−TS5−M6−TS6−M4

The highest energy barriers in these three pathways are defined by the TS4, TS7, and TS5 transition states, respectively. Among these transition states, the TS4 has the lowest relative free energy of 25.83 kcal/mol (Table 3).

In the most general case, the mechanism of ring inversion can be classified as simultaneous, when all torsion angles change their sign at once (flat transition state), as sequential (stepwise), or as random. Presumably, the type of mechanism for **2** can be determined from the analysis of geometries of transition states by locating the most eclipsed angle, as it is usually done in the case of noncyclic molecules. However, in cyclic systems the eclipsed angle does not necessarily lead to a barrier (e.g., conformational exchange in cyclopentane[25] is a barrierless process and yet each of the five torsion angles in cyclopentane would pass an eclipsed angle at some point). To further support this approach for cyclic molecules such as **2**, we have analyzed the dynamics of internal torsion angles while a molecule passes through the energy barrier. This information can be extracted from the torsion angle amplitudes (maximum displacement from equilibrium) associated with the imaginary frequency of the transition state.[19b] Thus, the TS4 state had the largest imaginary frequency amplitude at the ω_5 torsion angle (Figure 10a), which is well correlated with the most planar segment of the ring in TS4 at the ω_5 torsion angle (4.3°).

Similarly to TS4, for the TS7 state, the highest energy point of the second pathway, is structurally and vibrationally analogous to the TS4 (Figures 10a, d). The only difference between the TS7 and TS4 is the orientation of the N2 nitrogen lone electron pair orientation, which is not directly involved in the dynamics around the ω_5 angle and which will be discussed further below.

The third pathway has two high energy transition states TS5 and TS6, which are correspondingly 1.46 and 0.35 kcal/mol above the TS4. As opposed to TS4 and TS7, the transition states TS5 and TS6 were the most planar at the ω_3 (−26.6°) and ω_7 (11.2°) torsion angles, respectively (Table 3). However, even though these angles are far from being eclipsed, the imaginary frequency amplitudes were the largest at ω_3 in TS5 and at ω_7 in TS6 (parts b and c, respectively, of Figure 10). Interestingly, a single inversion of either the ω_3 or ω_7 torsion angle does not lead to a complete transition from one atropisomer to the other. Only consecutive sign
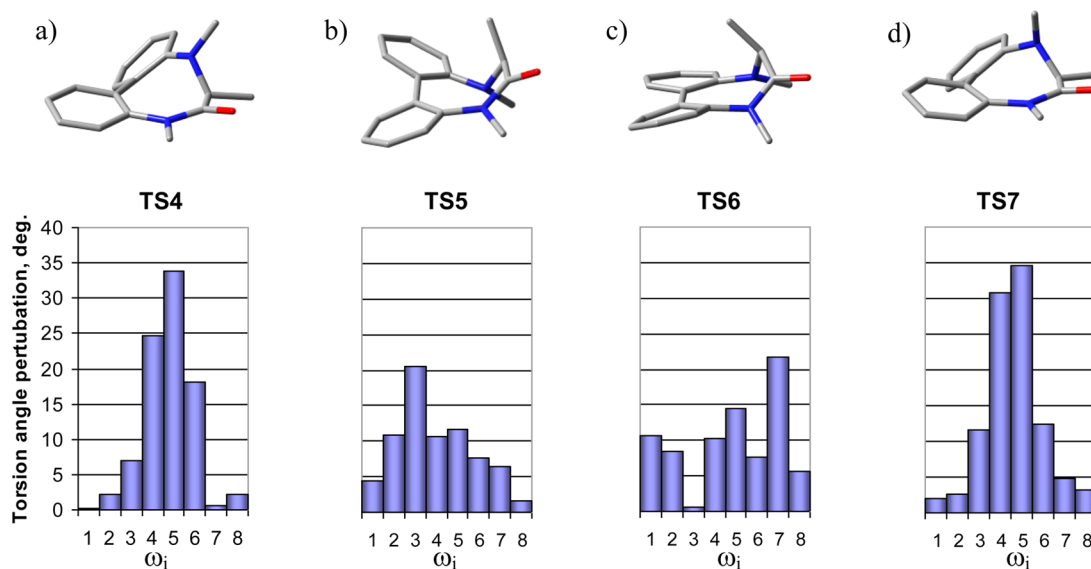

Figure 10. Optimized geometries (top) and torsion angle amplitudes (absolute values) associated with imaginary frequencies of the TS4−TS7 transition states of **2**.
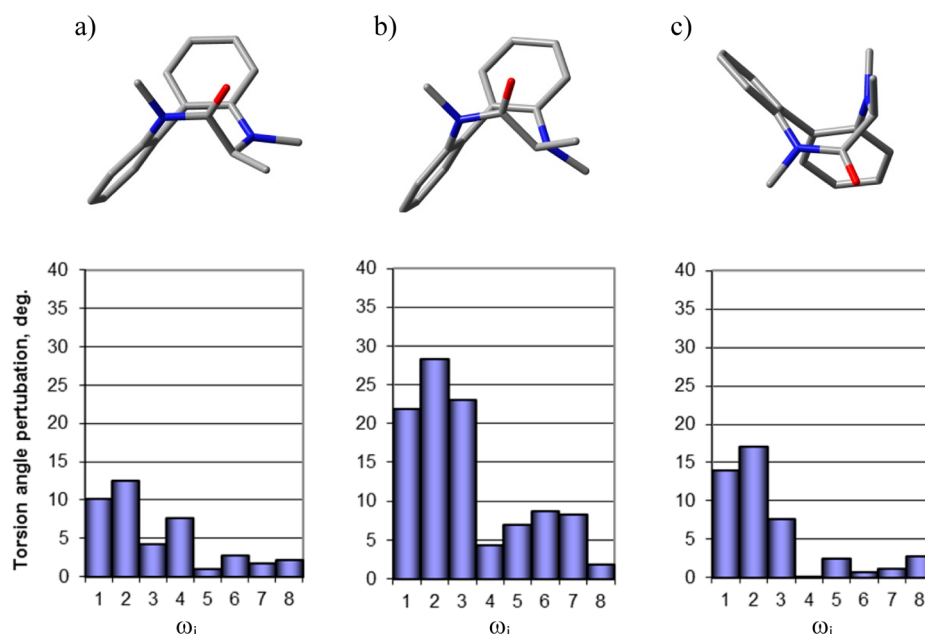
Figure 11. Optimized geometries (top) and torsion angle amplitudes (absolute values) associated with imaginary frequencies of the TS1–TS3 transition states of **2**.

inversions of both these angles, separated by the intermediate metastable high energy minimum M6, would achieve a complete atropisomerization.

Finally, there are three activation energies (TS1, TS2, and TS3) that describe transitions within each of the two families of conformations. These barriers are rather low and they do not exceed 5.3 kcal/mol (Table 3, Figure 11).

The TS1 and TS3 transition states are associated with pyramidal inversion of the N2 nitrogen, which is consistent with the largest vibrational amplitude at the ω_2 torsion angle (Figures 11a, c). The predicted free energies of activation for that process for **2** correlate well with those generally observed for tertiary amines.[26] Similar to the TS1 and TS3 transition states, the TS2 state is also characterized by the vibrational maximum at the ω_2 angle; however, its magnitude is almost twice as large as those of TS1 and TS3 (Figure 11b). The latter can be explained by the fact that the TS2 state is associated with the interconversion between the two gauche conformations with different ω_2 signs. In contrast to that, the extent of the ω_2 perturbation due to pyramidal inversion of the N2 nitrogen mediated by the TS1 and TS3 states is far less and does not involve sign inversion of the adjacent torsion angles.

Experimental NMR study of the low energy barriers, such as TS1, TS2, and TS3, would require very low temperature experiments (i.e., −180 °C and below), which were beyond the scope of the current study.

Interestingly, the highest barrier in the most feasible atropisomerization pathway I is not related to the steric and electronic interactions between the two aryl rings but to the interaction between the aryl and amide groups. This observation is somewhat inconsistent with the barriers expected for these groups in an open-chain molecule. Thus, DFT calculation (B3LYP/6-31G(d)) of Gibbs free activation energies corresponding to ω_7, ω_5, and ω_3 fragments of **2**, N2,N2,N2′,N2′-tetramethyl-1,1′-biphenyl-2,2′-diamine (**3**), N-methyl-N-phenylacetamide (**4**), and 2-(dimethylamino)-N,N-dimethylpropanamide (**5**), with torsion angles in transition

states close to those found in **2**, predicted 25.6, 10.4, and 8.5 kcal/mol, respectively.
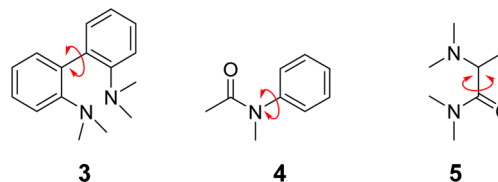
As expected for open-chain systems, the highest barrier within these three fragments was indeed predicted for the biaryl **3**. Surprisingly, this barrier is nearly identical to that of the TS4 energy; however, the latter might be expected to be better approximated by **4**. These results clearly indicate a potentially complex, nonlinear, and interdependent nature of the different types of barriers when those are grouped into a compact cyclic structure. Clearly more research is needed to understand this effect in more detail.

Another interesting observation that was surprising was the existence of two distinct atropisomerization pathways with rather similar barriers, but with two different sets of transition states. The origin of this interesting phenomenon is further examined in the next section.

Mechanism of Atropisomer Interconversion. It is clear that in the process of atropisomer interconversion of **2** all four dominant torsion angles change their sign by going through four eclipsed conformations ($\omega_i = 0$). Each of these conformations can be a potential transition state. However, the three pathways that have been described thus far showed that not all eclipsed conformations are transition states and, moreover, in some cases only two transition states separated atropisomers (i.e., pathway I with TS1 and TS4 states). Thus, to better understand the differences between different atropisomerization pathways and the mechanism of atropisomerization in general we have analyzed the dependencies of torsion angle changes along each of the three pathways.
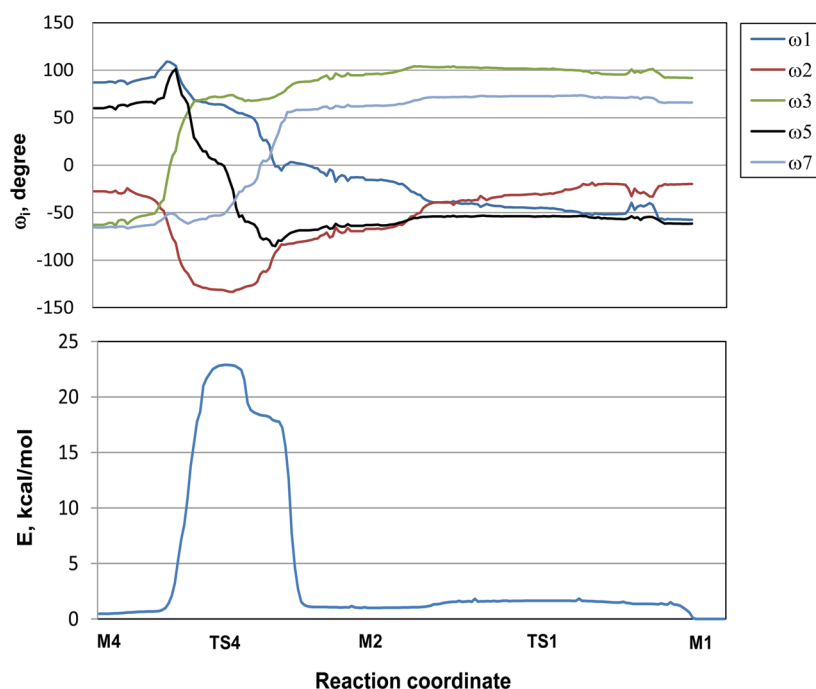
Figure 12. Torsion angle (top) and electron energy (bottom) dependencies along the internal reaction coordinate between the M1 and M4 states via pathway I.

The forward M1 to M4 interconversion along the path I (II) was initiated by the M1−TS1−M2 transition (Figure 9), which is predominantly associated with the N2 nitrogen pyramidal inversion. That transition does not involve the inversion of dominant torsion angles; nonetheless, it results in a significantly increased puckering at the ω_2 angle (−69.2°, Table 3). In nearly all lowest energy conformations of **2**, adjacent torsion angles or two torsion angles separated by a constrained angle (ω_4, ω_6, or ω_8) have alternative signs (Table 3). Therefore, it is not surprising that the increased negative value of the ω_2 angle in M2 form is compensated by a significant decrease of the adjacent negative ω_1 angle close to the planar value (−13.3°). The further progress toward the TS4 transition state is associated with increased negative value of the ω_2 (−130.9°) and with sign inversions of both ω_1 and ω_7 angles (compare M2 and TS4 forms in Table 3). It is difficult to determine whether inversions of ω_1 and ω_7 angle signs is a consecutive or synchronous process as both these events are barrierless, and yet closeness to planarity of the ω_1 in M2 that precedes the TS4 state slightly favors consecutive over synchronous inversion. Then, at the TS4 transition state, ω_5 inverts its sign (Table 3, Figure 10a), followed by a barrierless inversion of the ω_3 angle and by flattening of the ω_2 angle, which concludes the M1 to M4 transformation. That sequence of events can be schematically represented by the following notation

$$M1 \rightarrow (2)_0^- \rightarrow [(1)_-^+ \rightarrow (7)_+^-] \rightarrow (5)_-^+$$
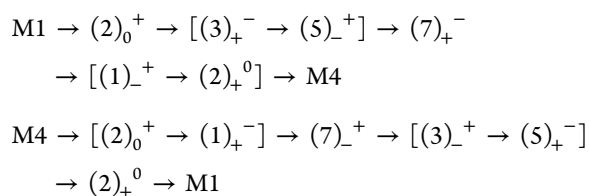$$\rightarrow [(3)_+^- \rightarrow (2)_-^0] \rightarrow M4$$
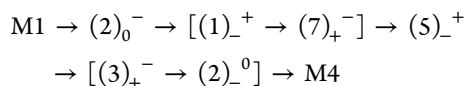
where the numbers in parentheses correspond to torsion angles; subscript and superscript indexes are initial and final signs of that angle, and transitions combined in square brackets are either consecutive or synchronous. Similarly, the reverse atropisomer interconversion from M4 to M1 along the path I (II) can be described as follows:

$$M4 \rightarrow (2)_0^- \rightarrow [(3)_-^+ \rightarrow (5)_+^-] \rightarrow (7)_-^+$$
$$\rightarrow [(1)_+^- \rightarrow (2)_-^0] \rightarrow M1$$
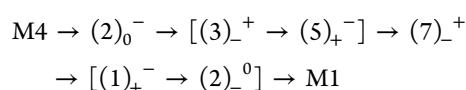
The eclipsed angle rotation along the 8-membered ring can be also gleaned from changes of torsion angles in the process of energy minimization starting from the transition states. Since such a minimization process is trying to follow the fastest descent to a minimum, it is reasonable to assume that the corresponding pathway would be a good approximation of the internal reaction coordinate (IRC) path.[27] Torsion angle trajectories along the pathway I for **2**, reconstructed from four energy minimization calculations originated from the TS1 and TS4 transition states in both directions, are shown in Figure 12 (see a 3D animation of the M4 to M1 interconversion via pathway I in the Supporting Information).

As seen in Figure 12, torsion angles in the vicinity of the T4 state consecutively $\omega_3 \rightarrow \omega_5 \rightarrow \omega_7 \rightarrow \omega_1$ pass zero values, while the ω_2 angle remains at its high values throughout the whole transition process. This observation strengthens the suggestion that the mechanism of atropisomer interconversion can be described by a consecutive inversion of dominant torsion angles along the ring. This conclusion has been further supported by the analysis of the pathway III.

Unlike pathways I and II, the forward M1 to M4 interconversion along pathway III is initiated by the positive ω_2 angle puckering after passing through the TS2 transition state (Figures 9 and 11b). Then, at the TS5 state, the signs of ω_3 and ω_5 angles are inverted (Table 3, Figure 10b), which is followed by the inversion of the ω_7 sign at the TS6 state (Table 3, Figure 10c). After that, a barrierless inversion of the ω_1 angle and reduced puckering of the ω_2 angle complete the atropisomer interconversion. Direct and reverse interconversions along the pathway III can be described by the following sign inversion sequences:

$$M1 \rightarrow (2)_0^+ \rightarrow [(3)_+^- \rightarrow (5)_-^+] \rightarrow (7)_+^-$$
$$\rightarrow [(1)_-^+ \rightarrow (2)_+^0] \rightarrow M4$$

$$M4 \rightarrow [(2)_0^+ \rightarrow (1)_+^-] \rightarrow (7)_-^+ \rightarrow [(3)_-^+ \rightarrow (5)_+^-]$$
$$\rightarrow (2)_+^0 \rightarrow M1$$

Thus, in general, the forward M1 to M4 and the reverse M4 to M1 atropisomer interconversions mediated by the pathway I (II) and III can be described as a consecutive process of torsion angle sign inversions in counterclockwise and clockwise directions correspondingly (i.e., rotation of eclipsed conformation), as shown in Figure 13. It is

Path I (II): M1 → M4

Path III: M4 → M1
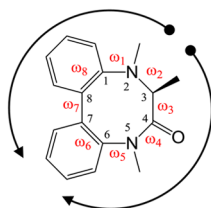
Path I (II): M4 → M1

Path III: M1 → M4

Figure 13. Arrows indicate directions of rotation of eclipsed conformation (torsional angle sign inversions) in the process of the M1 ↔ M4 atropisomer interconversion.

noteworthy that the three transition states, TS4, TS5, and TS6, associated with eclipsed conformations at three different segments of the ring corresponding to the three dominant torsion angles.

To accommodate a partial planarity of the ring in its transition state, the other segments of the ring should undergo a significant puckering. In all three cases, the largest puckering is observed at the ω_2 torsion angle, which reaches $-130.9°$ in TS4, $113.8°$ in TS5, and $117.4°$ in TS6 (Table 3). A unique flexibility of the ring at the ω_2, which can be attributed to the nature of the sp^3-sp^3 N2−C3 bond and the fact that both adjacent to the ω_2 torsional angles, and hence ω_1 and ω_3, are not constrained, are the essential features of 2 that define a transition state energy and the rate at which ring interconversion occurs. It is also noteworthy that the path III

forward and reverse interconversions proceed in the directions opposite to those of paths I and II (Figure 13). It appears that the type of a pathway is strongly depends of the directionality in which the sign of the ω_2 is initially perturbed and of the type of configuration of the state from which it starts.

The consecutive nature of torsion angle sign inversions along the ring in 2 somewhat resembles the pseudorotational mechanism of conformational exchange in other cyclic systems that was first introduced for 5-membered rings.[22,25] In both cases, there is no angular momentum associated with that rotation, and therefore, they can be classified as pseudorotation (false rotation). However, in the case of 5-membered rings, the pseudorotation is described as a rotation of the puckering coordinate along the ring, and it encompasses all endocyclic torsion angles, whereas in the case of 2 the position of the largest puckering remains constant (ω_2) and the eclipsed coordinate instead rotates around the ring and affects only the four dominant torsion angles. Another distinction between the 5-membered ring and the current system is the height of the barriers. In the former system, the barrier of pseudorotation is very low (<5 kcal/mol), whereas the currently studied 8-membered ring is characterized by a substantially higher barriers, which led to the observed atropisomerism.

In summary, the mechanism of atropisomer interconversion of 2 can be explained by the consecutive inversions of four dominant endocyclic torsion angles (ω_1, ω_3, ω_5, and ω_7) in either the clockwise or counterclockwise direction around the ring. The interconversion process is initiated by an increased puckering in the most flexible segment of the molecule (ω_2) that consequently facilitates the propagation of sign inversions in either clockwise or counterclockwise directions depending on the type of axial configuration of the initial state and the sign of the ω_2 puckering.

Atropisomer Interconversion via *trans*-Amide Conformations. DFT-calculated Gibbs free energies of the *trans*-amide conformations of 2 (M7−M12) were more than 15 kcal/mol higher than *cis*-amide forms (Table 3), which suggests these forms are unlikely intermediates of the atropisomer interconversion with an infinitely small probability of being detected experimentally. However, since the
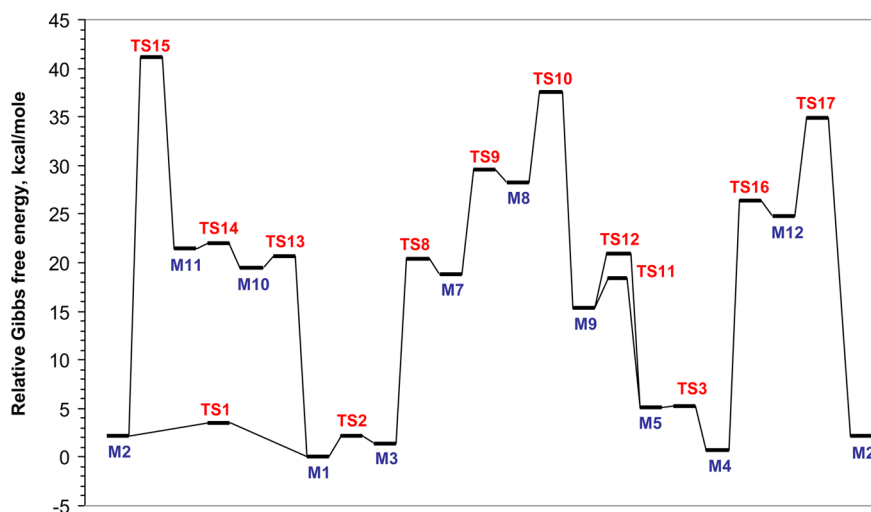

Figure 14. Energy profile for the interconversion process between the *cis*-amide (M1−M5) and *trans*-amide (M7−M12) conformations of 2.
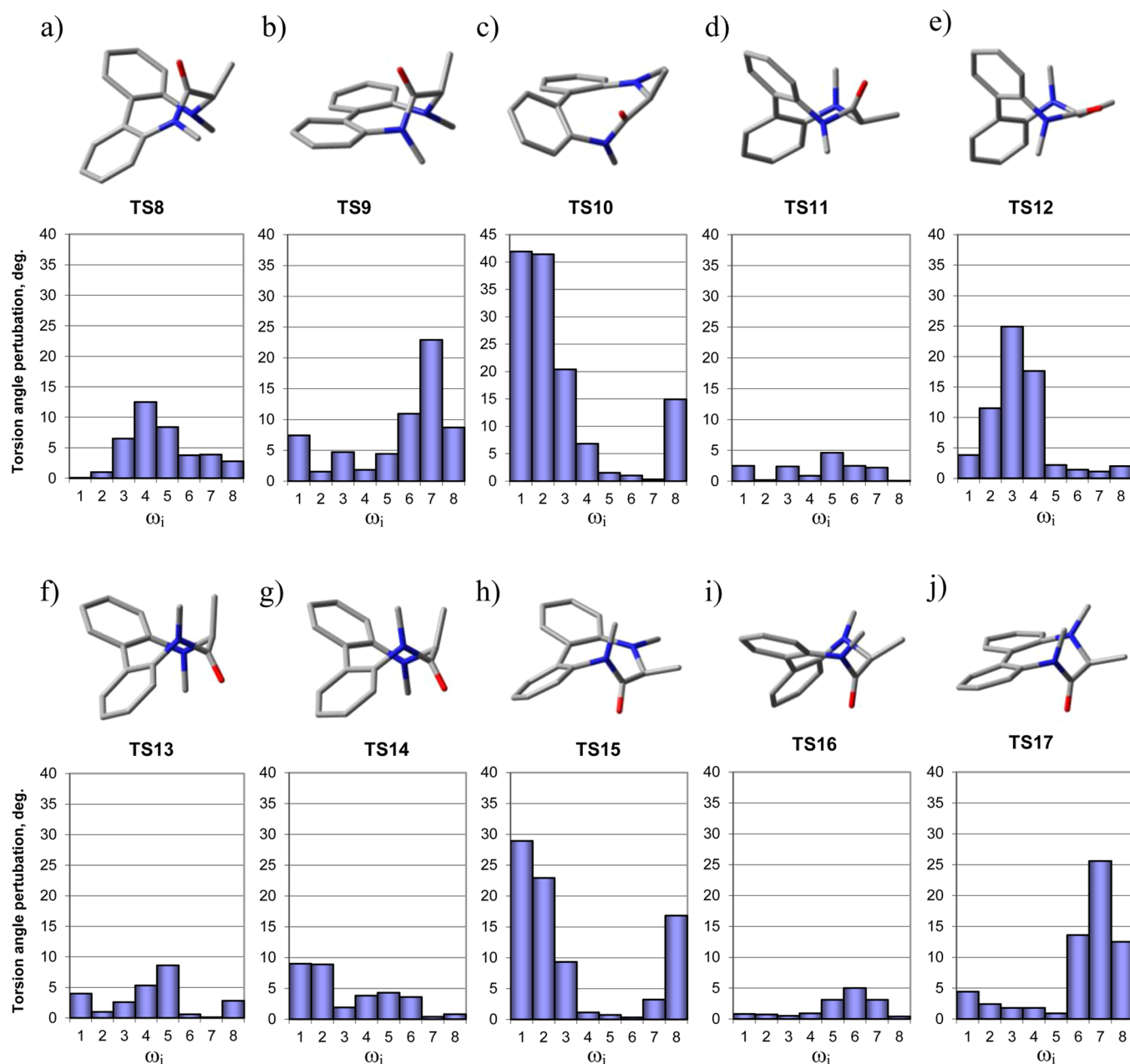
Figure 15. Optimized geometries (top) and torsion angle amplitudes (absolute values) associated with imaginary frequencies of the TS8−TS17 transition states of **2**.

energies of *trans*-amide conformations are still below the lowest atropisomeric barrier of *cis*-amide conformations (25.8 kcal/mol, TS4), the possibility of an alternative route of atropisomerization through *trans*-amide forms should be considered

$$c\text{-}(P, S) \leftrightarrow t\text{-}(P, S) \leftrightarrow t\text{-}(M, S) \leftrightarrow c\text{-}(M, S)$$

where c and t prefixes refer to *cis*- and *trans*-amide bond isomers, respectively.

2D PES scans and QST2 calculations predicted six ground states (M7−M12) and 10 transition states (T8−T17) that involved *trans*-amide conformations, which constituted three different pathways (Figure 14):
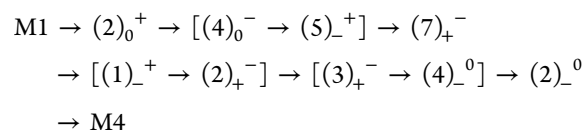
Path IV: M1−TS2−M3−TS8−M7−TS9−M8−TS10−M9−TS11−(TS12)−M5−TS3−M4

Path V: M1−TS1−M2−TS17−M12−TS16−M4

Path VI: M1−TS13−M10−TS14−M11−TS15−M2

Among these three pathways only the pathway IV follows the atropisomer interconversion route with the conserved *trans*-amide bond. In the other two pathways, either the *trans*-amide form is not preserved along the whole path (V) or it does not lead to the other atropisomer (VI).

Pathway IV, which encompasses the *trans*-amide conformation throughout the atropisomer interconversion, has numerous similarities with pathways via *cis*-amide conformations. Interestingly, for pathway IV one may also observe an eclipsed angle pseudorotation (Table 3):
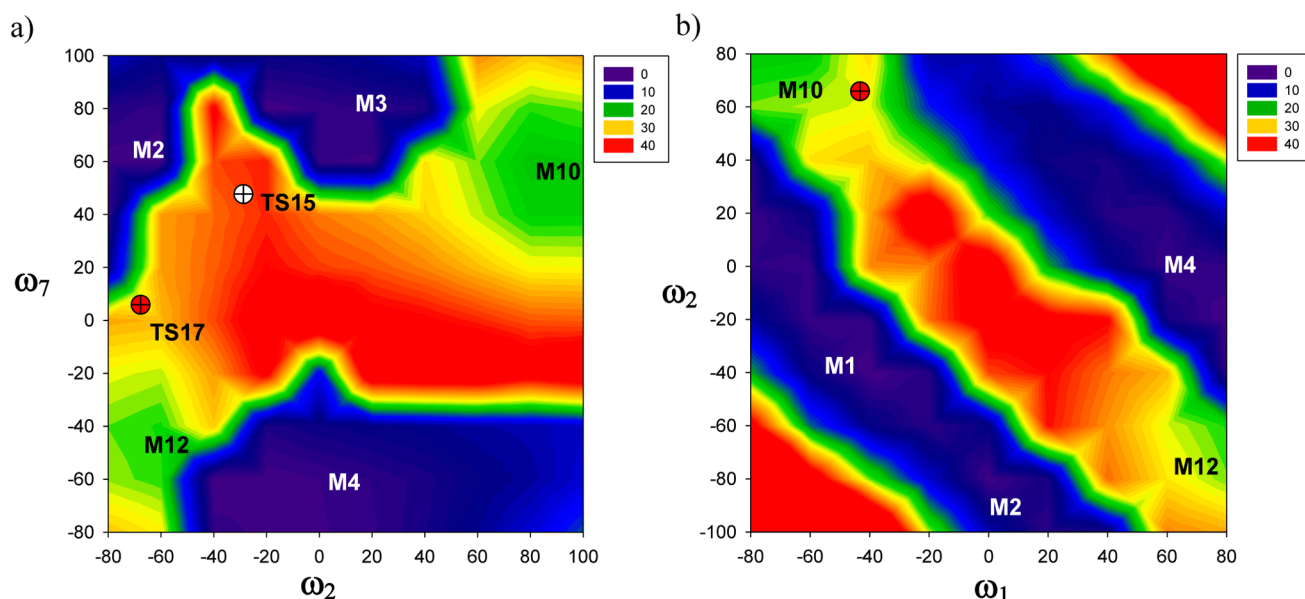
$$M1 \rightarrow (2)_0^+ \rightarrow [(4)_0^- \rightarrow (5)_-^+] \rightarrow (7)_+^-$$
$$\rightarrow [(1)_-^+ \rightarrow (2)_+^-] \rightarrow [(3)_+^- \rightarrow (4)_-^0] \rightarrow (2)_-^0$$
$$\rightarrow M4$$

Figure 16. 2D PES of the M12 to M10 interconversion in (ω_2, ω_7) (a) and (ω_1, ω_2) (b) coordinate space.

In terms of the directionality of pseudorotation of the eclipsed coordinate, pathway IV is similar to pathway III. However, in pathway III all transition states are exclusively puckered at the ω_2 angle, whereas in pathway IV that feature belongs to the *trans*-amide bond (ω_4). In all *trans*-amide conformations, ω_2 is forced out of planarity and becomes one of the three dominant torsional angles (ω_1, ω_2, and ω_7) which invert their signs upon atropisomerization. Even though the number of dominant torsion angles and the position of these angles are different in these two pathways, the directionality of pseudorotation still depends of the sign of the most puckered angle (ω_2 in pathways I−III and ω_4 in IV).

It is noteworthy that the initial step of *cis*- to *trans*-amide bond interconversions is a synchronous process where the change of the sign of the ω_4 angle is coupled with the inversion of the sign of the adjacent torsional angle in such a way that the sign alternation among endocyclic torsion angles is preserved. For example, when the ω_4 angle becomes negative in the *trans*-amide M7 form (M3 → M7), the adjacent angle, which was negative in the *cis*-M3 form (ω_5), synchronously inverts its sign to a positive value in the trans forms (and vice versa, when ω_4 becomes positive in M10 (M1 → M10), a positive adjacent angle (ω_3) in *cis*-M1 inverts its sign to negative in M10). Sign inversion upon *cis*- to *trans*-amide bond interconversion sets up the directionality of the eclipsed angle pseudorotation. Another difference between pathways III and IV is the number of transition states, which in the case of pathway IV is twice as many as for pathway III. Unlike pathway III, each pass of the eclipsed conformation along pathway IV has an energy barrier that is associated with certain transition state: TS8, ω_4 (ω_5); TS9, ω_7; TS10, ω_1 (ω_2); and TS11, TS12, ω_3 (ω_4). The latter can be readily followed by torsion angle amplitudes associated with corresponding imaginary frequencies (Figure 15).

As has been already mentioned, there are two types of *trans*-amide conformations distinguished by the sign of the ω_4 torsion angle (negative in M7, M8, and M9, and positive in M10, M11, and M12). Pathway IV encompasses conformations with only negative ω_4 angles. We were expecting a similar pathway for positive ω_4 conformations. However,

neither 2D PES nor the QST2 analyses revealed a transition state between the *t*-(*P*,*S*) M10 (M11) and *t*-(*M*,*S*) M12 forms. To further explore that pathway we have calculated 2D PES's between the M12 and M10 conformations in the (ω_1, ω_2) and (ω_2, ω_7) coordinate space, as shown in Figure 16 (since forward and reverse driven PES scans were nearly identical, only f-PES's are shown). As is clear from the 2D PES shown in Figure 16, there is no uninterrupted pathway between the two *trans*-amide conformations without descending into a *cis*-amide form (M1, M2, and M3). Thus, the whole pathway of atropisomer interconversion for the ω_4 positive *trans*-amide forms is reduced to two pathways, V and VI.

The IRC-type analysis of the TS17 transition state of the pathway V has confirmed that once the sign of the ω_7 angle is inverted by passing through the TS17 state (from the M12 side) the *trans*- to *cis*-amide isomerization of the (*P*,*S*) isomer is a barrierless process. Pathway VI does not involve atropisomer interconversion at all and can be described as follows:

$$c\text{-}(P,S) \leftrightarrow t\text{-}(P,S) \leftrightarrow t\text{-}(P,S)' \leftrightarrow c\text{-}(P,S)'$$

Interestingly, the TS15 state in pathway VI has the highest activation energy of **2** found thus far (41.11 kcal/mol), and it is not related to the atropisomer exchange but rather to the *cis*/*trans* isomerization of the amide bond of molecules with the same (*P*,*S*) configuration (Figure 14).

Thus, there are two pathways of atropisomer interconversion of **2** that encompass *trans*-amide bond conformations. Pathway IV conserves the *trans*-amide form along the entire atropisomerization path, with the highest transition state, TS10, at 37.6 kcal/mol (Figure 14). The TS10 state corresponds to the synchronous sign inversions of the two adjacent torsion angles ω_1 and ω_2. Pathway V proceeds via the TS1, TS17, and TS16 transition states with the *trans*-amide form, M12, representing a local minimum between the TS16 and TS17 states. The TS17 at 34.9 kcal/mol corresponds to the highest point on pathway V and is associated with the ω_7 sign inversion. Once that state is passed (from the M12 to M10 direction), the *trans*-amide isomerizes to the *cis*-amide without any barrier, as predicted

Table 4. Experimental and Calculated (For Pathway I, TS4) Gibbs Free Activation Energies, Enthalpy, and Entropy Contributions for (P,S) M1 to (M,S) M4 Atropisomerization

	experiment				calculations			
	$\Delta G_{298}^{\ddagger}$ (kcal/mol)	$\Delta H^{\ddagger}$ (kcal/mol)	$\Delta S^{\ddagger}$ (cal/(K mol))	ΔG_{PM}^{0} (kcal/mol)	$\Delta G_{298}^{\ddagger}$ (kcal/mol)	$\Delta H^{\ddagger}$ (kcal/mol)	$\Delta S^{\ddagger}$ (cal/(K mol))	$\Delta G_{M1,M4}^{0}$ (kcal/mol)
M4 → M1	25.59 ± 0.02	22.9 ± 0.02	−9.0 ± 0.7	−1.18 ± 0.04	25.0	22.4	−9.15	−0.76[a]
M1 → M4	26.77 ± 0.02	24.5 ± 0.02	−7.6 ± 1.1		25.8	23.1	−8.82	

[a]ΔG_{PM}^{0} calculated for the ensemble of M1−M5 conformations is −0.82 kcal/mol.

by the DFT calculations. Both pathways IV and V have barriers substantially higher than any of those with *cis*-amide conformations, and therefore, in practice, the *trans*-amide-mediated pathways are the least probable ones.

Despite the fact that our search for the *trans*-amide-mediated pathways of atropisomer inversion for **2** was not as exhaustive as the one for the family of *cis*-amide conformations, it seems reasonable to conclude that energetically there is no apparent reason for atropisomer inter-conversion to follow the path via *trans*-amide conformations. The activation energy to pass the eclipsed conformation is nearly independent from the amide bond isomerism. That extra barrier added to the high free energy of the *trans*-amide form constitutes an insurmountable apex with infinitely low probability that it will be passed at ambient temperatures.

Comparison of DFT Calculations with Experimental Results. Among the five pathways of atropisomerization of **2**, pathway I was found to be the most feasible one with the top saddle point at 25.8 kcal/mol associated with the inversion of the ω_5 torsion angle (TS4). Energetically, the closest pathway is III with the top TS5 saddle point (ω_3 inversion) 1.47 kcal/mol higher. The energy of the other transition state in pathway I (TS1) is five times lower than that of TS4. It has a minimal effect on atropisomerization rate of **2**, and therefore, it was neglected in the current discussion.

When the Gibbs free activation energies, activation enthalpy, and activation entropy were calculated for pathway I (TS4), those values showed good concurrence with the values for these parameters derived by the Eyring equation from experimental NMR data (Table 4). The largest part of the Gibbs free activation energy is associated with the activation enthalpy $\Delta H^{\ddagger}$, which is analogous to the butyl-bridged biphenyl atropisomerization[11a] and can be explained by increased molecular strain in the transition state due to bond bending and van der Waals repulsions. Thus, comparing the 8-membered ring endocyclic bond angles between ground states and transition state TS4, substantial angular perturbations were registered. The largest difference of 14.3° was observed for the ∠N5−C6−C7 bond angle. Then the interatomic distances between the aromatic H16 proton and two N5-methyl protons as well as the distance between one of the N5-methyl protons and carbonyl oxygen in TS4 transition state were 1.94, 2.03, and 2.01 Å, respectively. These distances are much shorter than the corresponding distances in M1 and M4 ground states (2.5−3.5 Å) and also much less than the sums of van der Waals radii of hydrogen (1.10 Å)[28a] and oxygen (1.52 Å).[28b] Therefore, it is not surprising that the largest strains in TS4 were found in the most planar part of the molecule (ω_5), which is also characterized by the largest torsion angle amplitudes at the imaginary frequency.

Entropic contributions to Gibbs free activation energy are rather minor, about 10%, and associated with some (about 9 eu) decrease of entropy of the activation state (Table 4).

Thermochemical DFT calculations[29] confirmed that translational, electronic, and rotational partition functions of entropy were nearly identical in the ground and transition states, whereas the vibrational partition function for the transition state declined. The latter is the result of the reduced number of low frequency normal modes in the transition state in comparison with that in ground states M1 and M4.

Calculated relative Gibbs free energy of the M1 and M4 forms ($\Delta G_{M1,M4}^{0} = -0.76$ kcal/mol) and averaged for the ensemble of (P,S) and (M,S) conformations ($\Delta G_{PM}^{0} = -0.82$ kcal/mol) showed an adequate agreement with the experimentally obtained data ($\Delta G_{PM}^{0} = -1.18$ kcal/mol). It should be noted that although the DFT analysis was performed on a molecular model with reduced substituents, the congruence between experimental and calculated Gibbs free energies, free activation energies, activation enthalpies, and activation entropies proved that that assumption to minimize the substituents was well justified.

In an attempt to have a better approximation of the free activation energies, the thermodynamic parameters of the stationary points of the pathways I−III were also recalculated using (a) a polarizable continuum model (PCM)[30] with the dielectric constant for toluene ($\varepsilon = 2.37$) at the B3LYP/6-31G(d) level of theory, (b) a dispersion-corrected B3LYP-D2[31] functional and 6-31G(d,p) basis set, and (c) a meta exchange-correlation M06-2X[32] functional and 6-31G(d,p) basis set (see the Supporting Information). The solvent-corrected calculations showed a better fit of the calculated free activation energy of the TS4 state ($\Delta G_{298}^{\ddagger} = 26.1$ kcal/mol) although relative Gibbs free energy between the M1 and M4 forms was less accurate ($\Delta G_{M1,M4}^{0} = -0.59$ kcal/mol). An analogous trend was observed for thermodynamic parameters calculated with the dispersion-corrected B3LYP-D2 functional (TS4: $\Delta G_{298}^{\ddagger} = 26.2$ kcal/mol, $\Delta G_{M1,M4}^{0} = -0.53$ kcal/mol), whereas M06-2X/6-31G(d,p) calculations predicted a slightly lower barrier and smaller relative free energy of the M1 and M4 forms (TS4: $\Delta G_{298}^{\ddagger} = 25.3$ kcal/mol, $\Delta G_{M1,M4}^{0} = -0.65$ kcal/mol). It is noteworthy that the most accurate estimation of the relative Gibbs free energies of (P,S) and (M,S) atropisomers was established with the dispersion-corrected B3LYP-D2/6-31G(d,p) calculations of 105 conformations of **1**. Thus, the calculated averaged ΔG_{PM}^{0} value of −1.28 kcal/mol was in nearly perfect agreement with the experimental value (−1.18 ± 0.04 kcal/mol) (see the Supporting Information for more details).

■ **CONCLUSIONS**

Gibbs free activation energy, activation entropy, and activation enthalpy of atropisomerization of **1** (Table 2) were estimated by using the Eyring equation from temperature-dependent kinetic NMR data.

Theoretical analysis of the atropisomerization of **1** was based on the DFT analysis (B3LYP/6-31G(d)) of two-

dimensional potential energy surfaces in endocyclic torsion coordinates of the 8-membered dibenzolactam **2**, a minimal substituent analogue of experimentally studied **1**. This approach led to the discovery of a conformationally rich landscape composed of 29 stationary points lying en route along five different pathways between the two lowest energy diastereotopic atropisomers. The current study at the DFT level of theory showed that the previously determined by force field approach two major conformations of (*P,S*) and (*M,S*) atropisomers of **1**[12a] were, in fact, two ensembles of eight and four ring conformations, respectively (or an ensemble of approximately 105 conformations if rotamers of the side chains of **1** were included). Among these 12 energy minima, there were five low energy forms (three (*P, S*) and two (*M,S*)) and seven forms with substantially higher energies. Most of the high energy forms have *trans*-amide bonds within the 8-membered ring that caused the Gibbs energy rise by 15 kcal/mol or more.[33] DFT-predicted relative Gibbs free energy of (*P,S*) and (*M,S*) atropisomers of **2** −0.82 kcal/mol and −1.28 kcal/mol calculated for 105 conformations of **1** at the B3LYP-D2/6-31G(d,p) level of theory were consistent with experimental −1.18 kcal/mol.

Conformational diversity of **2** was also the reason for 17 transition states that were ascertained through the DFT-based 2D PES and QST2 analysis. Fourteen transition states were directly involved in five different pathways between the two lowest energy atropisomer conformations. Among the five pathways, the lowest energy path was found through transition state TS4 with the DFT-estimated free activation energy of 25.8 kcal/mol (in vacuo) or 26.1 kcal/mol (PCM, toluene), which are in good agreement with the experimentally measured barrier (26.8 kcal/mol). Theoretical activation enthalpies and entropies were also consistent with experimental (Table 4), signifying the predominance of the enthalpy factor in the Gibbs free activation energy.

On the basis of the analysis of torsion angles of stationary points along the five pathways and torsional angle perturbations associated with imaginary frequencies of transition states, the mechanism of atropisomer interconversion through a stepwise propagation of the eclipsed angle along the 8-membered ring was proposed. Two major atropisomerization pathways are associated with the clockwise and counterclockwise rotation of the eclipsed angle, with one being slightly more accessible (by 1.46 kcal/mol). Unexpectedly, the highest transition state of the most feasible atropisomerization pathway was not defined by the steric and electronic properties of the biaryl fragment but rather by the lactam amide and phenyl interactions. It also became clear that the overall barrier of atropisomerization also depended upon the ability of the ring to accommodate a large puckering at one of the segments of the dibenzolactam ring. Introduction of structural changes, which would restrain or facilitate such flexibility (e.g., around ω_2 in **1**), would be a straightforward way to influence the rate of atropisomerization.

We believe that the analysis of mechanism of atropisomer interconversion of the studied dibenzolactam offers important insights into the dynamics of cyclic dibenzolactam and affords a better understanding of the factors that are critical for the atropisomerism in this and related systems.[1b,10,12b] The barrier of atropisomerization can be influenced by local structural changes in those parts of the ring that are critical for high atropoisomeric barriers. This knowledge provides researchers

with the tools for better predictions and potential modifications of molecular properties, such as bioavailability, solubility, toxicity, and efficacy. Moreover, this type of knowledge can find application in other fields where atropisomerization processes need to be assessed, such as organic catalysis and molecular electronics.

■ EXPERIMENTAL SECTION

Atropisomers of **1** were synthesized and separated chromatographically as previously described,[12a,b] and 20 mM solutions in toluene-d_8 were prepared for kinetic NMR measurements. ^{1}H NMR spectra were recorded on a 600 MHz spectrometer equipped with a 3 mm inverse detection probe. A freshly prepared sample of **1** with 95% of the (*M,S*) atropisomer was placed into a temperature-stabilized NMR spectrometer either at 34.2, 47.8, or 61.4 °C. Temperatures were calibrated using a methanol standard temperature calibration sample. Spectra with 16 scans with a 3 s delay and 3 s acquisition time were run every 10, 20, 30 min and then hourly for a period ranging from 22 to 65 h depending on the temperature of the experiment. Integral intensities of the well-resolved H9 proton resonances of two atropisomers at 6.3−6.5 ppm were used to monitor kinetics of atropisomer interconversion (Figure 2).

Experimental Kinetics. Kinetic data at three temperatures (Figure 2, Table 1) were analyzed by using KinFit program (D. V. Dearden, Brigham Young University, Provo, UT) in approximation of the first-order kinetic, (*M,S*)↔(*P,S*). KinFit program solves a set of coupled ordinary differential equations[34] and determines the best fit to the raw data by adjusting the rate constants using the Marquardt minimization algorithm.[35] Gibbs free activation energies ($\Delta G^{\ddagger}$), activation entropy ($\Delta H^{\ddagger}$), and activation enthalpy ($\Delta S^{\ddagger}$) (Tables 1, 2) were calculated from the temperature-dependent kinetics data by using the Eyring equation[14]

$$k = k_b T/h \, \exp(-\Delta G^{\ddagger}/RT)$$
$$= k_b T/h \, \exp(-\Delta H^{\ddagger}/RT + \Delta S^{\ddagger}/R)$$

where k is the kinetic rate constant, k_b is Boltzmann's constant, h is Planck's constant, and R is the gas constant. Calculation of thermodynamic parameters were done with the Solver tool of Microsoft Excel (2010).

Potential Energy Surface and TS calculations. Two-dimensional (2D) PES's (Figure 7) were calculated on a 20° grid by a systematic variation of two torsion angles while all other internal coordinates were optimized (i.e., relaxed PES). Initially, the pass from one minimum to the other was achieved by simultaneous change of the two given torsion angles (diagonal points of 2D PES). Then the columns of PES were calculated starting from the diagonal points by incrementing a torsion angle along the *y*-axis in both positive and negative directions. Once the diagonal points were calculated, points along the columns were calculated simultaneously by utilization of parallel computing on a Linux cluster, thus making the total time required for calculations of a single 2D PES only twice as long as of the time required to calculate diagonal elements of PES.

In addition to 12 PES scans that were calculated to follow atropisomer interconversion between the M1 to M4 conformations, we have also calculated four PES's to probe atropisomer interconversion mediated by a newly discovered trans-amide forms of **2**.

2D PES's allowed visualization of a minimum energy path from one atropisomer to the other and thus helped to define approximate locations of transition states, which were further employed as starting geometries in the Berny optimization algorithm[36] that searches for a saddle point with a single imaginary frequency. The imaginary frequency was then probed to ensure that the transition state indeed connected the two minima in question by the method similar to the internal reaction coordinate (IRC) approach.[24] For that purpose, two structures with positive and negative displacements along the vibration coordinate of the imaginary frequency were used as starting geometries in the energy minimization procedure. The

transition state was confirmed when these energy minimization calculations led to the two expected minima. In those cases when energy minimization would lead to the other than expected energy minimum, the quadratic synchronous transit-guided method (QST2)[23] was utilized to search for a new transition state between that and a target minimum. The last two steps were repeated until the target global minimum was reached. Frequency analyses were also applied to verify lowest energy states (all real frequencies) and to calculate the free energies which included scaled zero-point energies and thermal terms.[27] Unless otherwise stated, all DFT calculations were carried out at the B3LYP/6-31G(d) level of theory[37] by the Gaussian03[38a] and Gaussian09[38b] software packages. It has been verified that the calculations by both packages produced identical results. Trial calculations demonstrated that the differences in energy estimations between the two packages were less than 0.002 kcal/mol.

NMR Data. ^1H and ^{13}C chemical shifts and J_{HH} couplings of (P,S) and (M,S) of **1** were identical to those previously published.[12b] 2D homonuclear COSY and NOESY and heteronuclear HSQC, HSQCTOCSY and HMBC experiments were used for ^1H and ^{13}C resonance assignments.[12a]

(P,S)-7,8-Diallyl-5-benzyl-7,8-dihydrodibenzo[e,g][1,4]diazocin-6(5H)-one: δ_H (CDCl$_3$, 600 MHz) 7.40 (1H, td, *J* = 7.5, 1.8 Hz, H-17), 7.36 (1H, td, *J* = 7.5, 1.7 Hz, H-13), 7.26 (1H, dd, *J* = 1.8, 7.4 Hz, H-12), 7.18 (1H, td, *J* = 7.6, 1.8 Hz, H-7), 7.17 (1H, dd, *J* = 7.7, 1.5 Hz, H-15), 7.12 (1H, tt, *J* = 1.8, 7.3 Hz, H-21), 7.07 (1H, dd, *J* = 1.6, 8.0 Hz, H-6), 7.02 (2H, t, *J* = 7.8 Hz, H-20 and H20′), 6.85 (1H, td, *J* = 7.5, 1.7 Hz, H-8), 6.81 (2H, d, *J* = 7.8 Hz, H-19), 6.35 (1H, dd, *J* = 1.8, 7.5 Hz, H-9), 5.79 (1H, m, H-26), 5.55 (1H, m, H-23), 5.07 (1H, dq, *J* = 17.3, 1.8 Hz, H-27A), 5.04 (1H, bd, *J* = 10.3 Hz, H-27B), 4.97 (1H, d, *J* = 14.3 Hz, H-17A), 4.87 (1H, dq, *J* = 17.0, 1.7 Hz, H-24A), 4.84 (1H, bd, *J* = 9.9 Hz, H-24B), 4.44 (1H, d, *J* = 14.3 Hz, H-17B), 3.83 (1H, dd, *J* = 3.5, 9.7 Hz, H-3), 3.38 (1H, ddt, *J* = 5.1, 14.9, 1.6 Hz, H-22A), 3.28 (1H, dd, *J* = 7.9, 14.9 Hz, H-22B), 2.82 (1H, m, H-25A), 2.45 (1H, m, H-25B); δ_C (CDCl$_3$, 150 MHz) 170.3 (C-2), 147.7 (C-5), 140.9 (C-11), 140.3 (C-16), 136.5 (C-18), 136.3 (C-10), 135.26 (C-23), 135.1 (C-26), 130.8 (C-12), 130.8 (C-9), 130.1 (C-6), 128.84 (C-19), 128.83 (C-14), 128.5 (C-7), 128.1 (C-20), 127.7 (C-13), 127.0 (C-21), 125.8 (C-15), 125.0 (C-8), 116.9 (C-27), 116.6 (C-24), 63.9 (C-3), 57.7 (C-22), 52.3 (C-17), 36.7 (C-25).

(M,S)-7,8-Diallyl-5-benzyl-7,8-dihydrodibenzo[e,g][1,4]diazocin-6(5H)-one: δ_H (CDCl$_3$, 600 MHz) 7.40 (1H, td, *J* = 7.5, 1.6 Hz, H-17), 7.35 (1H, td, *J* = 7.5, 1.4 Hz, H-13), 7.26 (1H, td, *J* = 1.6, 7.3 Hz, H-7), 7.23 (1H, dd, *J* = 7.8, 1.4 Hz, H-15), 7.19 (1H, dd, *J* = 8.1, 1.3 Hz, H-6), 7.17 (1H, tt, *J* = 1.4, 7.5 Hz, H-21), 7.12 (1H, dd, *J* = 1.8, 7.5 Hz, H-12), 7.08 (2H, t, *J* = 7.6 Hz, H-20 and H20′), 6.87 (1H, td, *J* = 7.4, 1.3 Hz, H-8), 6.81 (2H, d, *J* = 7.9 Hz, H-19), 6.47 (1H, dd, *J* = 1.6, 7.4 Hz, H-9), 5.80 (1H, m, H-26), 5.45 (1H, m, H-23), 5.10−5.15 (2H, m, H-27), 4.91 (1H, d, *J* = 14.2 Hz, H-17A), 4.87−4.93 (2H, m, H-24), 4.38 (1H, d, *J* = 14.2 Hz, H-17B), 3.97 (1H, dd, *J* = 5.1, 10.5 Hz, H-3), 3.78 (1H, ddt, *J* = 6.7, 15.6, 1.4 Hz, H-22A), 3.59 (1H, ddt, *J* = 4.2, 15.6, 2.0 Hz, H-22B), 2.40 (1H, m, H-25A), 2.05 (1H, m, H-25B); δ_C (CDCl$_3$, 150 MHz) 169.8 (C-2), 147.7 (C-5), 140.7 (C-11), 140.2 (C-16), 136.7 (C-10), 136.5 (C-18), 135.4 (C-23), 134.0 (C-26), 129.3 (C-19), 128.9 (C-12), 128.64 (C-7), 128.59 (C-9), 128.1 (C-14), 128.0 (C-20), 127.5 (C-13), 127.1 (C-21), 125.9 (C-15), 123.9 (C-8), 122.5 (C-6), 117.4 (C-27), 116.6 (C-24), 73.6 (C-3), 54.7 (C-22), 54.5 (C-17), 35.8 (C-25).

ASSOCIATED CONTENT

Ⓢ Supporting Information

The Supporting Information is available free of charge on the ACS Publications website at DOI: 10.1021/acs.joc.5b02321.

Cartesian coordinates and energies for M1−M12 and TS1−TS17, relative Gibbs free energies of stationary points of **2** for pathways I−III, relative Gibbs free

energies of 105 conformations of **1**, and ^1H and ^{13}C NMR spectra for **1** (PDF)

3D animation of the M4 to M1 interconversion via pathway I (MPG)

AUTHOR INFORMATION

Corresponding Author

*E-mail: alexei.buevich@merck.com.

Notes

The authors declare no competing financial interest.

REFERENCES

(1) (a) Williams, D. H.; Bardsley, B. *Angew. Chem., Int. Ed.* **1999**, *38*, 1172. (b) Kupchan, S. M.; Britton, R. W.; Ziegler, M. F.; Gilmore, C. J.; Restivo, R. J.; Bryan, R. F. *J. Am. Chem. Soc.* **1973**, *95*, 1335. (c) Boyd, M. R.; Hallock, Y. F.; Cardellina, J. H., II; Manfredi, K. P.; Blunt, J. W.; McMahon, J. B.; Buckheit, R. W., Jr.; Bringmann, G.; Schäffer, M.; Cragg, G. M.; Thomas, D. W.; Jato, J. G. *J. Med. Chem.* **1994**, *37*, 1740.

(2) (a) Carini, D. J.; Duncia, J. V.; Aldrich, P. E.; Chiu, A. T.; Johnson, A. L.; Pierce, M. E.; Price, W. A.; Santella, J. B., III; Wells, G. J.; Wexler, R. R.; Wong, P. C.; Yoo, S.−E.; Timmermans, P. B. M. W. M. *J. Med. Chem.* **1991**, *34*, 2525. (b) Aulakh, G. K.; Sodhi, R. K.; Singh, M. *Life Sci.* **2007**, *81*, 615.

(3) (a) Evans, B. E.; Rittle, K. E.; Bock, M. G.; DiPardo, R. M.; Freidinger, R. M.; Whitter, W. L.; Lundell, G. F.; Veber, D. F.; Anderson, P. S.; Chang, R. S. L.; Lotti, V. J.; Cerino, D. J.; Chen, T. B.; Kling, P. J.; Kunkel, K. A.; Springer, J. P.; Hirshfieldt, J. *J. Med. Chem.* **1988**, *31*, 2235. (b) Welsch, M. E.; Snyder, S. A.; Stockwell, B. R. *Curr. Opin. Chem. Biol.* **2010**, *14*, 347.

(4) (a) Lloyd-Williams, P.; Giralt, E. *Chem. Soc. Rev.* **2001**, *30*, 145. (b) Bringmann, G.; Price Mortimer, A. J.; Keller, P. A.; Gresser, M. J.; Garner, J.; Breuning, M. *Angew. Chem., Int. Ed.* **2005**, *44*, 5384.

(5) Mishchenko, A.; Zotti, L. A.; Vonlanthen, D.; Burkle, M.; Pauly, F.; Cuevas, J. C.; Mayor, M.; Wandlowski, T. *J. Am. Chem. Soc.* **2011**, *133*, 184.

(6) (a) Eliel, E. L.; Wilen, S. H.; Mander, L. N. *Stereochemistry of Organic Compounds*; John Wiley and Sons, 1994; pp 1142−1145. (b) Oki, M. *Top. Stereochem.* **1984**, 1.

(7) (a) Putey, A.; Popowycz, F.; Do, Q.-T.; Bernard, P.; Talapatra, S. K.; Kozielski, F.; Galmarini, C. M.; Joseph, B. *J. Med. Chem.* **2009**, *52*, 5916. (b) Chobanian, H. R.; Guo, Y.; Liu, P.; Lanza, T. J., Jr.; Chioda, M.; Chang, L.; Kelly, T. M.; Kan, Y.; Palyha, O.; Guan, X.-M.; Marsh, D. J.; Metzger, J. M.; Raustad, K.; Wang, S.-P.; Strack, A. M.; Gorski, J. N.; Miller, R.; Pang, J.; Lyons, K.; Dragovic, J.; Ning, J. G.; Schafer, W. A.; Welch, C. J.; Gong, X.; Gao, Y.-D.; Hornak, V.; Reitman, M. L.; Nargund, R. P.; Lin, L. S. *Bioorg. Med. Chem.* **2012**, *20*, 2845. (c) LaPlante, S. R.; Edwards, P. J.; Fader, L. D.; Jakalian, A.; Hucke, O. *ChemMedChem* **2011**, *6*, 505.

(8) Leroux, F. *ChemBioChem* **2004**, *5*, 644.

(9) (a) Grein, F. *J. Phys. Chem. A* **2002**, *106*, 3823. (b) Arulmozhiraja, S.; Fujii, T. *J. Chem. Phys.* **2001**, *115*, 10589. (c) Arulmozhiraja, S.; Selvin, P. C.; Fujii, T. *J. Phys. Chem. A* **2002**,

106, 1765. (d) Karpfen, A.; Choi, C. H.; Kertesz, M. *J. Phys. Chem. A* **1997**, *101*, 7426.

(10) (a) Wong, G. T.; Manfra, D.; Poulet, F. M.; Zhang, Q.; Josien, H.; Bara, T.; Engstrom, L.; Pinzon-Ortiz, M.; Fine, J. S.; Lee, H.-J. J.; Zhang, L.; Higgins, G. A.; Parker, E. M. *J. Biol. Chem.* **2004**, *279*, 12876. (b) Tabata, H.; Suzuki, H.; Akiba, K.; Takahashi, H.; Natsugari, H. *J. Org. Chem.* **2010**, *75*, 5984. (c) Tabata, H.; Akiba, K.; Lee, S.; Takahashi, H.; Natsugari, H. *Org. Lett.* **2008**, *10*, 4871.

(11) (a) Bihlmeier, A.; Rotzler, J.; Rickhaus, M.; Mayor, M.; Klopper, W. *Phys. Chem. Chem. Phys.* **2015**, *17*, 11165. (b) Rotzler, J.; Gsellinger, H.; Bihlmeier, A.; Gantenbein, M.; Vonlanthen, D.; Häussinger, D.; Klopper, W.; Mayor, M. *Org. Biomol. Chem.* **2013**, *11*, 110. (c) Rotzler, J.; Gsellinger, H.; Neuburger, M.; Vonlanthen, D.; Haussinger, D.; Mayor, M. *Org. Biomol. Chem.* **2011**, *9*, 86.

(12) (a) Wang, C. H.; Reilly, J.; Brand, N.; Schwartz, S.; Alluri, S.; Chan, T. M.; Buevich, A. V.; Ganguly, A. K. *Tetrahedron Lett.* **2010**, *51*, 6213. (b) Wang, C. H.; White, A. R.; Schwartz, S. N.; Alluri, S.; Cattabiani, T. M.; Zhang, L. K.; Chan, T. M.; Buevich, A. V.; Ganguly, A. K. *Tetrahedron* **2012**, *68*, 9750.

(13) Bortolotti, L. J.; Flurchick, K. In *Reviews in Computational Chemistry*; Lipkowitz, K. B., Boyd, D. B., Eds.; VCH: New York, 1996; Vol. 7, Chapter 4.

(14) Eyring, H. *J. Chem. Phys.* **1935**, *3*, 107.

(15) Sherer, E. C.; Lee, C. H.; Shpungin, J.; Cuff, J. F.; Da, C.; Ball, R.; Bach, R.; Crespo, A.; Gong, X.; Welch, C. J. *J. Med. Chem.* **2014**, *57*, 477.

(16) Feuston, B. P.; Miller, M. D.; Culberson, J. C.; Nachbar, R. B.; Kearsley, S. K. *J. Chem. Inf. Model.* **2001**, *41*, 754.

(17) Blaney, J. M.; Crippen, G. M.; Dearing, A.; Dixon, J. S. *DGEOM; Quantum Chemistry Program Exchange*; Indiana University: Bloomington, 1990.

(18) (a) Hawkins, P. C.; Nicholls. *J. Chem. Inf. Model.* **2012**, *52*, 2919. (b) Hawkins, P. C.; Skillman, A. G.; Warren, G. L.; Ellingson, B. A.; Stahl, M. T. *J. Chem. Inf. Model.* **2010**, *50*, 572.

(19) (a) Schlegel, H. B. In *Modern Electronic Structure Theory*; Yarkony, D. R., Ed.; World Scientific Publishing: Singapore, 1995; pp 459−500. (b) Hratchian, H. P.; Schlegel, H. B. In *Theory and Applications of Computational Chemistry: The First Forty Years*; Dykstra, C., Frenking, G., Kim, K., Scuseria, G., Eds.; Elsevier, 2005; pp 195−249.

(20) (a) Koča, J. *Prog. Biophys. Mol. Biol.* **1998**, *70*, 137. (b) Fadrna, E.; Koča, J. *J. Phys. Chem. B* **1997**, *101*, 7863.

(21) Burkert, U.; Allinger, N. L. *J. Comput. Chem.* **1982**, *3*, 40.

(22) Burkert, U.; Allinger, N. L. *Molecular Mechanics ACS Monograph 177*; American Chemical Society: Washington, DC, 1982.

(23) (a) Peng, C.; Ayala, P. Y.; Schlegel, H. B.; Frisch, M. J. *J. Comput. Chem.* **1996**, *17*, 49. (b) Peng, C.; Schlegel, H. B. *Isr. J. Chem.* **1993**, *33*, 449.

(24) (a) Hendrickson, J. B. *J. Am. Chem. Soc.* **1967**, *89*, 7036. (b) Anet, F. L. *Top. Curr. Chem.* **1974**, *44*, 170.

(25) (a) Kilpatrick, J. E.; Pitzer, K. S.; Spitzer, R. *J. Am. Chem. Soc.* **1947**, *69*, 2483. (b) Pitzer, K. S.; Donath, W. E. *J. Am. Chem. Soc.* **1959**, *81*, 3213. (c) Cremer, D.; Pople, J. A. *J. Am. Chem. Soc.* **1975**, *97*, 1354. (d) Cremer, D.; Pople, J. A. *J. Am. Chem. Soc.* **1975**, *97*, 1358. (e) Cui, W.; Li, F.; Allinger, N. L. *J. Am. Chem. Soc.* **1993**, *115*, 2943. (f) Cornell, W. D.; Ha, M. P.; Sun, Y.; Kollman, P. A. *J. Comput. Chem.* **1996**, *17*, 1541.

(26) Lehn, J. M. *Top. Curr. Chem.* **1970**, *15*, 311.

(27) Fukui, K. *Acc. Chem. Res.* **1981**, *14*, 363.

(28) (a) Bondi, A. *J. Phys. Chem.* **1964**, *68*, 441. (b) Rowland, R. S.; Taylor, R. *J. Phys. Chem.* **1996**, *100*, 7384.

(29) Levine, I. N. *Quantum Chenistry*, 6th ed.; Prentice Hall: Upper Saddle River, 2009.

(30) Tomasi, J.; Mennucci, B.; Cammi, R. *Chem. Rev.* **2005**, *105*, 2999.

(31) Grimme, S. *J. Comput. Chem.* **2006**, *27*, 1787.

(32) Zhao, Y.; Truhlar, D. G. *Theor. Chem. Acc.* **2008**, *120*, 215.

(33) Interestingly, the *trans*-amide bond within a ring system does not always lead to a free energy elevation. Thus, the Gly-Gly-Gly 9-membered cyclic peptide has the lowest energy conformation with two *cis*- and one *trans*-amide bond (Tosso, R. D.; Zamora, M. A.; Suvire, F. D.; Enriz, R. D. *J. Phys. Chem. A* **2009**, *113*, 10818). A smaller ring size of **1**, along with the constraints of the embedded biphenyl moiety, effectively prevent an optimal 180° angle of the trans-amide bond that can only be attained with a significant energy penalty.

(34) Shampine, L. F.; Gordon, M. K. *Computer Solutions of Ordinary Differential Equations: The Initial Value Problem*; W. H. Freeman: San Francisco, 1975.

(35) Bevington, P. R.; and Robinson, D. K. *Data Reduction and Error Analysis for the Physical Sciences*; McGraw-Hill: New York, 1992.

(36) Schlegel, H. B. *J. Comput. Chem.* **1982**, *3*, 214.

(37) Frisch, M. J.; Pople, J. A.; Binkley, J. S. *J. Chem. Phys.* **1984**, *80*, 3265.

(38) (a) Frisch, M. J. et al. *Gaussian 03, Revision E.01*; Gaussian, Inc.: Wallingford, CT, 2004. (b) Frisch, M. J. et al. *Gaussian 09, Revision A.02*; Gaussian, Inc.: Wallingford, CT, 2009.